J. Fluid Mech. (2004), *vol.* 508, *pp.* 133–163.
DOI: 10.1017/S0022112004009000 Printed in the United Kingdom

The instability of thermal and fluid fronts during radial injection in a porous medium

By DAVID PRITCHARD

BP Institute for Multiphase Flow, University of Cambridge, Madingley Rise, Madingley Road, Cambridge CB3 0EZ, UK

(Received 5 August 2003 and in revised form 8 January 2004)

We investigate viscous fingering instabilities of the double-front system which results when fluid is injected into a porous medium containing fluid of a different composition and temperature. We describe a linear stability analysis based on an eigenfunction expansion method which enables us to investigate the structure of the discrete eigenvalue spectrum. We investigate the extent to which the properties of each front contribute to the tendency of the system to become unstable: we find that instabilities on the compositional front dominate because of the high ratio of thermal to solute diffusion. It is difficult for a stable compositional front to stabilize an unstable thermal front; however, this situation can result in a new fingering phenomenon in which the perturbations undergo coupled oscillations of growing amplitude.

1. Introduction

When fluid is injected into a porous medium which is already saturated with native fluid of a different temperature and composition, two travelling fronts develop. The first (the *compositional front* or *fluid front*) is the interface between injected and ambient fluid; depending on the properties of the fluids, this may be an immiscible front upon which capillary forces act, or a miscible front across which mechanical dispersion and molecular diffusion blend the fluid properties. The second front is the *thermal front*, which represents the point where the temperature of the fluid changes from the injectate temperature to the ambient temperature. Assuming local thermal equilibrium, the thermal front must travel more slowly than the fluid front, because heat must be shared with the porous matrix as well as with the fluid. This front is never sharp, because heat is redistributed across the front by dispersion and by diffusion through both the fluid and the solid phases.

In general, the mechanical properties of a fluid depend on both its composition and its temperature. In particular, we may expect the viscosity to change across each front, and this means that a fingering instability (Saffman & Taylor 1958; Homsy 1987) may develop on either front. The growth rate and preferred scale of the instability on each front is controlled by the viscosity contrast and by the diffusive redistribution of properties across the front; additionally, the dynamics of the two fronts are coupled, because each front is affected by the perturbations induced by the instability on the other front.

This process is of interest as a fundamental problem in fluid dynamics, with the feature that two instabilities with different preferred scales are strongly coupled. It also has direct applications to a variety of industrial and environmental processes where one fluid is injected into a reservoir of another: examples include enhanced oil recovery (Latil 1980) and geothermal reservoir recharge (Stefánsson 1997; Woods

1999). Additionally, this study provides a necessary precursor to investigating the stability of flow- and thermally driven chemical reaction fronts in porous media (Phillips 1991; French 2002; Jupp & Woods 2003), with wide-ranging applications in chemical and reservoir engineering as well as its intrinsic geological interest.

In this paper, we investigate the linear stability of the double-front system in the case in which the fluid front is miscible. This builds on a substantial literature on the instabilities of miscible fronts in porous media and Hele-Shaw cells, of which we summarize only a few of the more relevant studies here.

The first detailed analyses of the linear stability of a fluid front with miscible properties were carried out by Tan & Homsy (1986, 1987). Tan & Homsy (1986) considered rectilinear flow, and employed a quasi-steady approximation in which the growth rate of instabilities was asymptotically much faster than the rate of change of the background state: this allowed a favoured unstable wavelength to be identified at any point in 'frozen time'. A large number of studies have built on this approach, including effects such as buoyancy contrasts, tangential shear and non-Newtonian rheologies (Rogerson & Meiburg 1993; Manickam & Homsy 1995; Azaiez & Singh 2002).

Tan & Homsy (1987) considered the miscible displacement front resulting from radial injection. In this geometry, the basic state is dimensionally degenerate (in a sense which will be specified below), and as a result it is possible to transform the problem into similarity variables and abandon the quasi-steady assumption. This is an important difference, since experimental evidence suggests that in many situations the growth rate of instabilities is too small for the quasi-steady approximation to be valid, especially at early times when the diffusive front spreads rapidly.

Recently, Ben, Demekhin & Chang (2002) developed a method to circumvent the quasi-steady assumption for rectilinear flow by projecting the streamwise structure of the perturbation onto a suitable set of eigenfunctions. The key to this approach is that the first eigenfunction in the set describes an infinitesimal advance or delay of the spreading front, and it can be shown (Barenblatt 1996, § 8.3) that such perturbations to a self-similar solution can persist whereas all other forms of perturbation decay. Consequently, this single eigenfunction comes to dominate the structure of any growing perturbation, and Ben *et al.* employed this dominance to obtain asymptotic results for the linear stability of the front.

It is possible to develop a similar eigenfunction decomposition for radial flow, and this is the approach taken in the current paper. While it is no longer necessary to circumvent the quasi-steady assumption, the eigenfunction decomposition still has advantages over the usual semi-numerical approach. First, it makes explicit the physical meaning of the perturbation, which to leading order represents an infinitesimal advance or delay of the spreading front, as for immiscible displacements. Second, it naturally identifies not just a single perturbation growth rate but a complete spectrum.

The spectrum of growth rates is of particular interest in the light of the study by Cardoso & Woods (1995), who considered the stability of an expanding annulus of fluid formed by the sequential injection of immiscible fluids into a Hele-Shaw cell. In this study, distinct 'varicose' and 'sinuous' modes of instability were found, and the two modes could become unstable simultaneously. Although the stabilizing mechanisms and the precise geometry are different in the current study, the coupling of the instabilities on the two fronts is similar in several respects: we consider this similarity in § 3.

The current problem also has similarities to that investigated by Manickam & Homsy (1993), who considered situations in which the viscosity is a non-monotonic

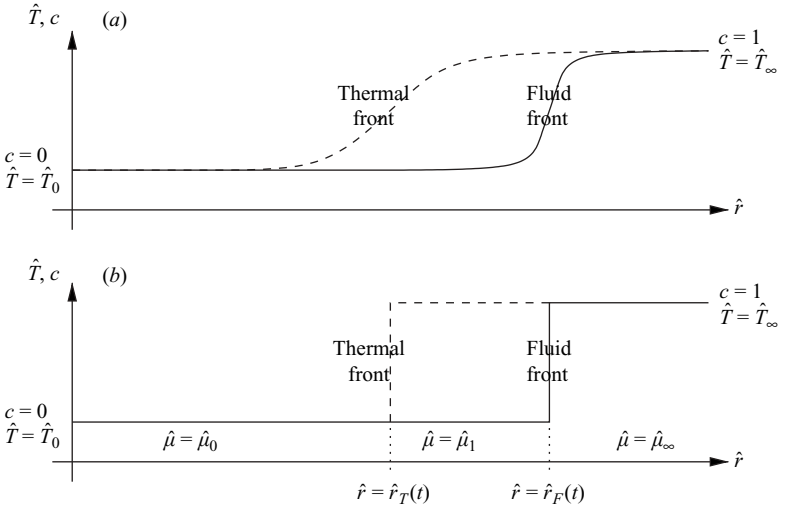

FIGURE 1. Schematic of 'double-front' structure for miscible fluids: solid line represents solute concentration c while dashed line represents temperature $\hat{T}$. (a) Front structure with thermal and solute diffusion; (b) 'thin front' approximation (§ 3).

function of solute concentration. However, the current study differs from this because the thermal and fluid properties diffuse and are advected at different rates, and this significantly affects the coupling of the frontal instabilities.

In § 2 we formulate the problem, and identify the governing dimensionless parameters. In § 3, we consider a schematic version of the problem in which the radial structure of the fronts is neglected. This demonstrates how the coupling between the instabilities is controlled by the relative speeds of the fronts and by the azimuthal wavelength of the perturbation. Section 4 describes the eigenfunction decomposition method used to set up the linear problem, and in § 5 we describe the results obtained using this approach for a number of physically interesting cases. In particular, we demonstrate how instabilities can come to be dominated by the properties of either the thermal or the fluid front, and we discuss the ability of one front to stabilize or destabilize the other. We summarize our findings in § 6.

2. Formulation

We consider the two-dimensional flow that results from the injection of fluid into a horizontal layer from a line source at position $\hat{r} = 0$; the azimuthal coordinate is denoted by θ. We describe the fluid composition in terms of a notional solute concentration c, which varies from 0 in the injected fluid to 1 in the ambient fluid, and we describe the fluid motion in terms of a transport velocity $\hat{\boldsymbol{u}} = (\hat{u}_r, \hat{u}_\theta)$. (Throughout, dimensional variables are denoted by a caret and dimensionless variables are unadorned.)

The fluid is injected at a constant areal flux $\hat{Q}$ and with temperature $\hat{T}_0$ and viscosity $\hat{\mu}_0$, while the ambient fluid far from the injection point has temperature $\hat{T}_\infty$ and viscosity $\hat{\mu}_\infty$. We assume that the grain size of the porous matrix is sufficiently small that the fluid and the matrix are in local thermal equilibrium with temperature $\hat{T}$. Figure 1 illustrates the double-front structure which results once the flow has become established.

The governing equations are given by mass conservation and Darcy's law in the radial and azimuthal directions,

$$\frac{1}{\hat{r}}\frac{\partial}{\partial \hat{r}}(\hat{r}\hat{u}_r)+\frac{1}{\hat{r}}\frac{\partial \hat{u}_\theta}{\partial \theta}=0, \quad \frac{\partial \hat{p}}{\partial \hat{r}}=-\frac{\hat{\mu}}{\hat{k}}\hat{u}_r, \quad \frac{1}{\hat{r}}\frac{\partial \hat{p}}{\partial \theta}=-\frac{\hat{\mu}}{\hat{k}}\hat{u}_\theta \tag{2.1}$$

(where $\hat{k}$ is the permeability of the porous medium), together with advection–diffusion equations for temperature $\hat{T}$ and for the concentration of solute c:

$$\frac{\partial \hat{T}}{\partial \hat{t}}+\frac{\lambda}{\phi}\hat{\boldsymbol{\nabla}}\cdot(\hat{\boldsymbol{u}}\hat{T})=\hat{\kappa}_T\hat{\nabla}^2\hat{T}, \quad \frac{\partial c}{\partial \hat{t}}+\frac{1}{\phi}\hat{\boldsymbol{\nabla}}\cdot(\hat{\boldsymbol{u}}c)=\hat{\kappa}_c\hat{\nabla}^2 c. \tag{2.2}$$

Here $\hat{\kappa}_T$ and $\hat{\kappa}_c$ are the effective diffusivities of heat and solute respectively: the ratio $E\equiv\hat{\kappa}_T/\hat{\kappa}_c$ is the Lewis number, which (following Jupp & Woods 2003) we expect to be much greater than unity. The parameter λ quantifies the thermal lag effect in a porous medium, and is defined as

$$\lambda=\frac{\phi_t\hat{\rho}_{\text{fluid}}\hat{C}_{\text{fluid}}}{\phi_t\hat{\rho}_{\text{fluid}}\hat{C}_{\text{fluid}}+(1-\phi_t)\hat{\rho}_{\text{matrix}}\hat{C}_{\text{matrix}}}<1 \tag{2.3}$$

(Jupp & Woods 2003). Here the total porosity of the matrix is denoted by ϕ_t, and $\hat{\rho}$ and $\hat{C}$ are the density and specific heat capacity of each phase. (We will denote the effective porosity, i.e. the fraction of connected void space, by ϕ.)

We assume that the changes to fluid density are sufficiently small that $\hat{\rho}_{\text{fluid}}$ and λ may be regarded as constants. However, the fluid viscosity $\hat{\mu}$ is taken to be a function of both temperature $\hat{T}$ and concentration c.

2.1. *Non-dimensionalization and basic states*

Since $\hat{Q}$, $\hat{\kappa}_T$ and $\hat{\kappa}_c$ have the same dimensions, there is no way to define intrinsic length- and timescales. To non-dimensionalize, then, we define an arbitrary lengthscale $\hat{r}_0$ and a corresponding timescale $\hat{t}_0=2\pi\hat{r}_0^2/\hat{Q}$. The value of $\hat{r}_0$ is immaterial, as the self-similarity of the basic solutions means that it can be eliminated by a simple rescaling (cf. Tan & Homsy 1987; Riaz & Meiburg 2003).

We define

$$\left.\begin{aligned} r&=\frac{\hat{r}}{\hat{r}_0}, \quad t=\frac{\hat{t}}{\hat{t}_0}, \quad u_r=\frac{\hat{u}_r\hat{t}_0}{\hat{r}_0\phi}, \quad u_\theta=\frac{\hat{u}_\theta\hat{t}_0}{\hat{r}_0\phi},\\ T&=\frac{\hat{T}-\hat{T}_0}{\hat{T}_\infty-\hat{T}_0}, \quad \mu=\frac{\hat{\mu}}{\hat{\mu}_0}, \quad p=\hat{p}\frac{2\pi\hat{k}}{\hat{\mu}_0\phi\hat{Q}} \end{aligned}\right\} \tag{2.4}$$

to obtain the non-dimensionalized governing equations

$$\frac{1}{r}\frac{\partial}{\partial r}(ru_r)+\frac{1}{r}\frac{\partial u_\theta}{\partial \theta}=0, \quad \frac{\partial p}{\partial r}=-\mu u_r, \quad \frac{1}{r}\frac{\partial p}{\partial \theta}=-\mu u_\theta, \tag{2.5}$$

$$\frac{\partial T}{\partial t}+\lambda\left[\frac{1}{r}\frac{\partial(ru_rT)}{\partial r}+\frac{1}{r}\frac{\partial(u_\theta T)}{\partial \theta}\right]=\frac{1}{P_T}\left[\frac{1}{r}\frac{\partial}{\partial r}\left(r\frac{\partial T}{\partial r}\right)+\frac{1}{r^2}\frac{\partial^2 T}{\partial \theta^2}\right], \tag{2.6}$$

$$\frac{\partial c}{\partial t}+\left[\frac{1}{r}\frac{\partial(ru_rc)}{\partial r}+\frac{1}{r}\frac{\partial(u_\theta c)}{\partial \theta}\right]=\frac{1}{P_c}\left[\frac{1}{r}\frac{\partial}{\partial r}\left(r\frac{\partial c}{\partial r}\right)+\frac{1}{r^2}\frac{\partial^2 c}{\partial \theta^2}\right], \tag{2.7}$$

where

$$P_T=\frac{\hat{Q}}{2\pi\hat{\kappa}_T}, \quad P_c=\frac{\hat{Q}}{2\pi\hat{\kappa}_c}. \tag{2.8}$$

P_T and P_c are the thermal and fluid Péclet numbers, which represent the ratio of advective to diffusive transport of heat and solute respectively.

We impose boundary conditions in the far field as $r \to \infty$ and at the origin $r = 0$, noting that the experiments of Woods & Fitzgerald (1997) have demonstrated that the similarity solution which gives the basic state for our analysis provides a good description of the injection process, and the flow rapidly becomes independent of the finite injection pipe width $r = r_1$.

For constant-flux injection, the boundary conditions in non-dimensional form are that

$$T = 0 \quad \text{and} \quad c = 0 \quad \text{at} \quad r = 0, \qquad \lim_{r \to 0} r u_r = 1, \tag{2.9}$$

$$T \to 1 \quad \text{and} \quad c \to 1 \quad \text{as} \quad r \to \infty. \tag{2.10}$$

The basic state which satisfies these conditions is taken to be independent of θ: it is given by $u_{rb} = 1/r$, and hence

$$T_b(r, t) = \frac{1}{K_T} \int_0^{\zeta} \mathrm{e}^{-P_T u} u^{\lambda P_T/2 - 1} \, \mathrm{d}u, \quad \text{where} \quad K_T = \frac{\Gamma\left(\frac{1}{2}\lambda P_T\right)}{P_T^{\lambda P_T/2}}, \tag{2.11}$$

$$c_b(r, t) = \frac{1}{K_c} \int_0^{\zeta} \mathrm{e}^{-P_c u} u^{P_c/2 - 1} \, \mathrm{d}u, \quad \text{where} \quad K_c = \frac{\Gamma\left(\frac{1}{2}P_c\right)}{P_c^{P_c/2}}, \tag{2.12}$$

where we have defined the similarity variable

$$\zeta = \frac{r^2}{4t}. \tag{2.13}$$

In equations (2.11) and (2.12), $\Gamma(x)$ is the standard gamma function: we note that T_b and c_b can be expressed in terms of incomplete gamma functions.

The quantities T_b and c_b are positive everywhere, varying from 0 at the injection point to 1 in the far field. (Because we have normalized temperature by the quantity $\hat{T}_\infty - \hat{T}_0$, which may be positive or negative, T is not necessarily of the same sign as $\hat{T} - \hat{T}_0$.) The fluid front is centred around $\zeta = \frac{1}{2}$, with its width in ζ-space proportional to $P_c^{-1/2}$; the thermal front is centred around $\zeta = \frac{1}{2}\lambda$, with its width in ζ-space proportional to $P_T^{-1/2}$.

Finally, we specify the dependence of viscosity on temperature and concentration. Following previous studies from Tan & Homsy (1987) onwards, we assume that the viscosity μ varies exponentially with both the temperature and the solute concentration,

$$\mu = \exp(-\beta_T T - \beta_c c). \tag{2.14}$$

The exponents β_T and β_c may be positive or negative. Negative values represent more-viscous fluid ahead of the front (and are therefore associated with instability); positive values represent less-viscous fluid ahead of the front.

3. The thin-front stability problem

Before formulating the full stability problem, we consider briefly the limiting case in which we neglect both diffusion and the radial structure of the background state, retaining only the destabilizing Saffman–Taylor mechanism and the coupling through the velocity field. These results demonstrate how the parameters λ and m control the

instability, and suggest some points which are useful in the physical interpretation of the results.

The structure considered in this section is illustrated in figure 1(*b*). The dimensionless viscosity of the fluid at the source is given by $\mu = \mu_0 = 1$; the viscosity in the far field is given by $\mu = \mu_\infty = \mathrm{e}^{-\beta_T - \beta_c}$, and the viscosity between the fronts is given by $\mu = \mu_1 = \mathrm{e}^{-\beta_T}$. (For convenience we also define the mobilities $M_i = \mu_i^{-1}$.) The fluid front is located at $r = r_F(t)$, and it is simple to show that $r_F(t) = \sqrt{2t}$, while the thermal front is located at $r = r_T(t) = \sqrt{2\lambda t}$.

We may employ the analysis by Paterson (1981) to obtain results for the stability of the fronts when coupling between them, as well as stabilizing effects such as diffusion and surface tension, are neglected. If the front positions are perturbed to $r_T(\theta, t) = \sqrt{2\lambda t} + \epsilon A(t)\mathrm{e}^{\mathrm{i}m\theta}$ and $r_F(\theta, t) = \sqrt{2t} + \epsilon B(t)\mathrm{e}^{\mathrm{i}m\theta}$, where $\epsilon \ll 1$ is the perturbation parameter and m is the azimuthal wavenumber, then the amplitudes $A(t)$ and $B(t)$ grow algebraically with time, $A(t) \sim B(t) \sim t^\omega$, in contrast to the exponential growth to be expected in a planar geometry. This means that the instability develops more slowly relative to the change of the background state, and that the most unstable wavenumber becomes dominant more gradually.

The growth rate on a front advancing as $\mathrm{d}r/\mathrm{d}t = \lambda/r(t)$ with viscosity μ_i behind and μ_j ahead is given by

$$\omega_{ij}(m) = \frac{1}{2}\left[m\frac{\mu_j - \mu_i}{\mu_j + \mu_i} - 1\right]. \tag{3.1}$$

We note that this result is independent of λ, because this factor occurs both in the denominator of ω_{ij} (through the radius of the front) and in the numerator, through the advective velocity driving the instability. Equation (3.1) differs from the Saffman–Taylor result for a planar front, because the velocity which forces the instability weakens as the front spreads.

To address the double-front problem, we follow the analysis of Cardoso & Woods (1995), with the exception that the kinematic condition at the thermal front is now given by $\mathrm{d}r_T/\mathrm{d}t = \lambda u_r(r_T, t)$. Applying the matching conditions on pressure and velocity across the interfaces in the absence of surface tension, we may obtain equations for the interface perturbation amplitudes $A(t)$, $B(t)$ of the form

$$t\frac{\mathrm{d}A}{\mathrm{d}t} = C_{11}(m)A + C_{12}(m)B, \qquad t\frac{\mathrm{d}B}{\mathrm{d}t} = C_{21}(m)A + C_{22}(m)B, \tag{3.2}$$

with solutions proportional to $t^{\omega_\pm}$, where

$$\omega_\pm = \tfrac{1}{2}\left[C_{11} + C_{22} \pm \sqrt{C_{11}^2 + C_{22}^2 - 2C_{11}C_{22} + 4C_{12}C_{21}}\right]. \tag{3.3}$$

The coefficients $C_{ij}(m)$ are given in Appendix A.

We may also obtain the eigenvectors (A, B) which correspond to these eigenvalues. The quantities $(A/B)_\pm$, which represent the ratio of the magnitudes of the perturbations on the thermal and fluid fronts, are given by

$$\left(\frac{A}{B}\right)_\pm = \frac{C_{11} - C_{22} \pm \sqrt{C_{11}^2 + C_{22}^2 - 2C_{11}C_{22} + 4C_{12}C_{21}}}{2C_{21}}. \tag{3.4}$$

If $(A/B) > 0$, the perturbations on the thermal and fluid fronts are in phase, giving the annulus of fluid between the fronts a sinuous structure (as described by Cardoso &

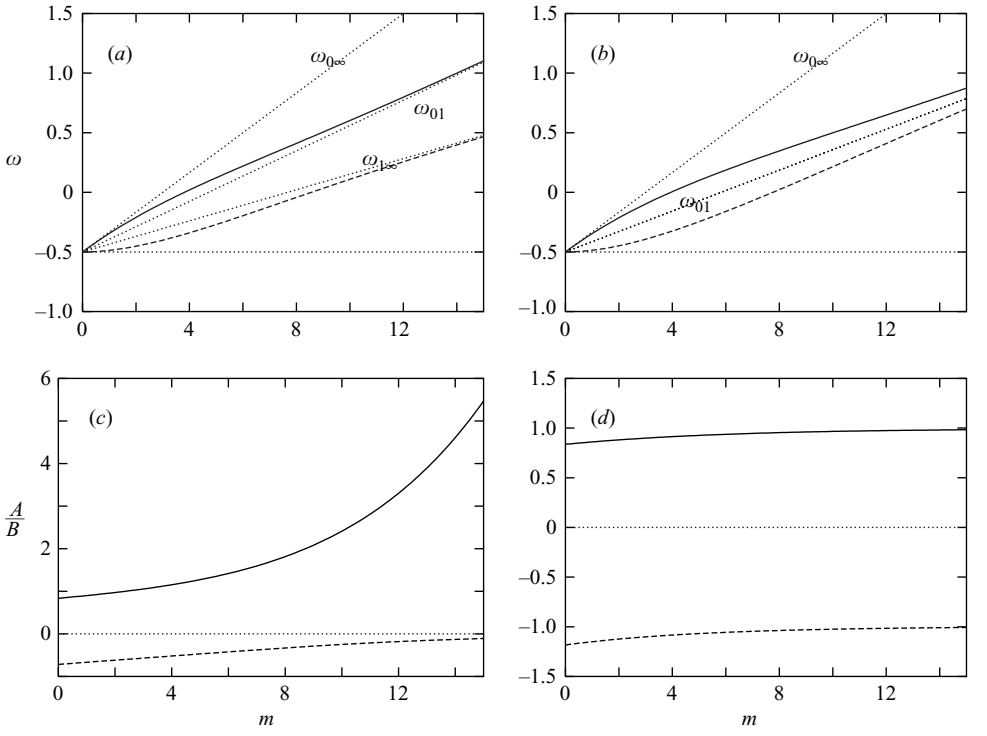

FIGURE 2. Eigenvalues $\omega_{\pm}$ and the corresponding ratios $(A/B)_{\pm}$ for cases where both thermal and fluid fronts are unstable. In each case solid lines correspond to ω_{+} and dashed lines to ω_{-}. (a,c) $M_1 = 0.65$, $M_\infty = 0.5$, $\lambda = 0.7$. (b,d) $M_1 = 1/\sqrt{2}$, $M_\infty = 1/2$, $\lambda = 0.7$ (so $\omega_{01} = \omega_{1\infty}$). Dotted lines (labelled) represent Saffman–Taylor results for single fronts.

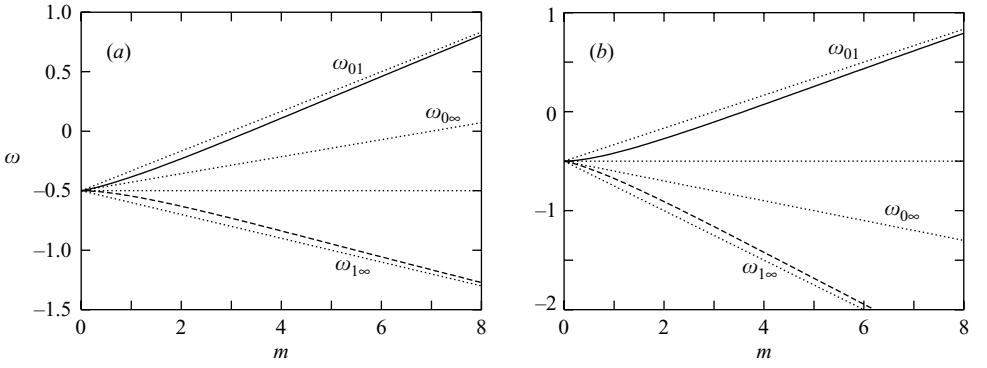

FIGURE 3. Eigenvalues $\omega_{\pm}$ for cases where only the thermal front is unstable. In each case solid lines correspond to ω_{+} and dashed lines to ω_{-}. (a) $M_1 = 0.5$, $M_\infty = 0.75$, $\lambda = 0.7$. (b) $M_1 = 0.5$, $M_\infty = 1.5$, $\lambda = 0.7$. Dotted lines (labelled) represent Saffman–Taylor results for single fronts.

Woods 1995). Conversely, if $(A/B) < 0$, the perturbations are out of phase, corresponding to a varicose perturbation to the annulus.

Some representative cases are shown in figures 2 and 3.

The coupling of the instabilities is controlled by λ, which dictates the spatial separation of the fronts, and m, which determines the spatial scale of the velocity

perturbation on each front. At low m and high λ there are strongly coupled 'global' modes, while at high m or low λ the perturbations become strongly localized around the fronts, and the eigenvalues $\omega_\pm$ asymptote to the single-thin-front growth rates (3.1) on each front. (When diffusion is included in the problem, we may expect that this will alter the growth rates most for high m, and so equation (3.1) may never provide an accurate estimate of the growth rate.)

Specifically, the asymptotic behaviour of the eigenvalues is given by

$$\omega_+ \sim \max\left(\omega_{0\infty}, -\tfrac{1}{2}\right) \quad \text{and} \quad \omega_- \sim \min\left(\omega_{0\infty}, -\tfrac{1}{2}\right) \qquad \text{as} \quad m \to 0, \tag{3.5}$$

$$\omega_+ \sim \max\left(\omega_{01}, \omega_{1\infty}\right) \quad \text{and} \quad \omega_- \sim \min\left(\omega_{01}, \omega_{1\infty}\right) \qquad \text{as} \quad m \to \infty. \tag{3.6}$$

When both fronts are unstable, ω_+ corresponds to a sinuous instability of the annulus and ω_- to a varicose instability; when only one front is unstable, both eigenvalues correspond to sinuous modes. For the special case of global instability when $\omega_{01} = \omega_{1\infty}$, the eigenvalues $\omega_\pm$ again correspond to sinuous and varicose perturbations respectively, but no longer localize on one interface or the other; rather, they represent the odd and even parts of a global perturbation of the annulus.

We can also use the result (3.3) to show that only real growth rates are permitted: the details are given in Appendix A. We will return to this point in § 5.3.2.

A final point which these results raise is the question of neutral stability. The algebraic growth rates described above are expressed in terms of the perturbation to the radial positions of the fronts $r_T(t)$ and $r_F(t)$. When the problem including diffusion is considered, it is natural to work in terms of the similarity variable $\zeta = r^2/(4t)$ (compare e.g. Tan & Homsy 1987), in which case the front positions are given by

$$\zeta_T(t) = \frac{1}{2}\lambda + \epsilon \frac{A(t)}{(2t)^{1/2}} \mathrm{e}^{\mathrm{i}m\theta}, \quad \zeta_F(t) = \frac{1}{2} + \epsilon \frac{B(t)}{(2t)^{1/2}} \mathrm{e}^{\mathrm{i}m\theta}. \tag{3.7}$$

Consequently, the growth rate of the perturbation to the front is different depending on whether it is viewed in the physical coordinates (r, t) or the similarity variables (ζ, t).

To interpret the results for the growth rate, then, it is useful to have two definitions of instability in mind: either $\omega > 0$, so the absolute size of the perturbations to the front position grows, or $\omega > \frac{1}{2}$, so the perturbations grow relative to the radius of the front. (The latter definition is employed by Tan & Homsy 1987.) This distinction does not arise in the case of a rectilinear front, because there is no longer a changing lengthscale perpendicular to the front.

Additionally, when we compare the discussion of a unidirectional diffusing front (see Barenblatt 1996, § 8.3), this suggests a third way of interpreting the growth rate. Barenblatt's general definition of the stability of an invariant solution suggests (as we shall see) that the perturbation as $m \to 0$ may be regarded as neutrally stable. In the current geometry, this would lead to a stability criterion of $\omega > -\frac{1}{2}$; for a planar front, it would again coincide with $\omega = 0$. This third definition has the advantage that it makes the interpretation of the eigenvalue spectrum $\omega(m)$ similar to that for the unidirectional front. It also provides the most cautious definition of stability, and we will use it when discussing the structure of the eigenvalue spectrum is subsequent sections; however, this subtlety of the physical interpretation should be borne in mind throughout.

4. The full linear stability problem

We now consider the full linearized stability problem when diffusion is included. We first formulate a perturbation expansion, and then describe the radial decomposition of the perturbation structure in terms of an appropriate set of eigenfunctions.

4.1. *Perturbation expansion*

We define a small parameter $\epsilon \ll 1$, and seek expansions of the form

$$\left.\begin{aligned} u_r &= u_{rb} + \epsilon e^{im\theta} U_1(r,t), \quad u_\theta = \epsilon e^{im\theta} W_1(r,t), \quad T = T_b + \epsilon e^{im\theta} T_1(r,t), \\ c &= c_b + \epsilon e^{im\theta} C_1(r,t), \quad \mu = \mu_b + \epsilon e^{im\theta} M_1(r,t), \quad p = p_b + \epsilon e^{im\theta} P_1(r,t), \end{aligned}\right\} \tag{4.1}$$

where the real parts of these expressions are assumed, and where we have defined the quantity $M_1(r,t)$ for convenience in what follows, although viscosity cannot be perturbed independently of T and c. We employ the periodicity of the disturbance in the azimuthal direction to expand it in Fourier modes, with wavenumbers $m \in \mathbb{N}$, and we will employ a representation of the radial structure which allows disturbances to be localized in r. We do not consider perturbations in the vertical direction, since the work of Riaz & Meiburg (2003) suggests that the presence of these perturbations does not alter the basic dynamics of miscible instability, but incorporating them does complicate the analysis substantially.

The boundary conditions are that the perturbations to the temperature and solute concentration fields vanish at the point of injection and far from the front; additionally, the perturbation to the radial flux of fluid, $2\pi r U_1$, must vanish in these limits (which is equivalent to requiring that the pressure perturbation P_1 must vanish). These can be written as

$$\left.\begin{aligned} T_1 &\to 0 \\ C_1 &\to 0 \\ rU_1 &\to 0 \end{aligned}\right\} \quad \text{as} \quad r \to 0 \quad \text{and as} \quad r \to \infty. \tag{4.2}$$

We may substitute the perturbations (4.1) into the non-dimensionalized governing equations (2.5), (2.6) and (2.7), expand in powers of ϵ, and eliminate W_1 and P_1 to obtain

$$\frac{\partial}{\partial r}\left[rU_1\mu_b + r^2\frac{\partial U_1}{\partial r}\mu_b\right] = m^2\mu_b U_1 + m^2\frac{M_1}{r}. \tag{4.3}$$

The advection–diffusion equations for temperature and solute concentration may also be expanded to first order in ϵ to yield

$$\frac{\partial T_1}{\partial t} + \lambda\left(U_1\frac{\partial T_b}{\partial r} + \frac{1}{r}\frac{\partial T_1}{\partial r}\right) = \frac{1}{P_T}\left[\frac{1}{r}\frac{\partial}{\partial r}\left(r\frac{\partial T_1}{\partial r}\right) - \frac{m^2}{r^2}T_1\right], \tag{4.4}$$

$$\frac{\partial C_1}{\partial t} + \left(U_1\frac{\partial c_b}{\partial r} + \frac{1}{r}\frac{\partial C_1}{\partial r}\right) = \frac{1}{P_c}\left[\frac{1}{r}\frac{\partial}{\partial r}\left(r\frac{\partial C_1}{\partial r}\right) - \frac{m^2}{r^2}C_1\right]. \tag{4.5}$$

We now define new dependent variables. First, the form of the boundary conditions (4.2) on U_1 suggests that we define a new quantity proportional to rU_1; in addition, motivated by the transformation which will be required in §4.2, we divide all the dependent quantities through by t, defining

$$\Upsilon(r,t) = rtU_1, \quad \Theta(r,t) = tT_1, \quad \chi(r,t) = tC_1, \quad N(r,t) = tM_1. \tag{4.6}$$

We then transform to the independent variables (ζ, t), where ζ is defined by equation (2.13), and employ the expressions (2.11) and (2.12) to obtain the equations

$$\frac{\partial}{\partial\zeta}\left[\zeta\mu_b(\zeta)\frac{\partial\Upsilon}{\partial\zeta}\right] = \frac{1}{4}m^2\mu_b(\zeta)\frac{\Upsilon}{\zeta} + \frac{1}{4}m^2\frac{N}{\zeta}, \tag{4.7}$$

$$t\frac{\partial\Theta}{\partial t} = \mathscr{L}_T\Theta - \frac{1}{4}\frac{m^2}{P_T}\frac{\Theta}{\zeta} - \frac{1}{2}\lambda\Upsilon\frac{1}{K_T}\mathrm{e}^{-P_T\zeta}\zeta^{\lambda P_T/2-1}, \tag{4.8}$$

$$t\frac{\partial\chi}{\partial t} = \mathscr{L}_c\chi - \frac{1}{4}\frac{m^2}{P_c}\frac{\chi}{\zeta} - \frac{1}{2}\Upsilon\frac{1}{K_c}\mathrm{e}^{-P_c\zeta}\zeta^{P_c/2-1}, \tag{4.9}$$

where the operators $\mathscr{L}_T$ and $\mathscr{L}_c$ are defined by

$$\mathscr{L}_T \equiv \left[\frac{\zeta}{P_T}\frac{\partial^2}{\partial\zeta^2} + \left(\frac{1}{P_T} - \frac{\lambda}{2} + \zeta\right)\frac{\partial}{\partial\zeta} + 1\right], \quad \mathscr{L}_c \equiv \left[\frac{\zeta}{P_c}\frac{\partial^2}{\partial\zeta^2} + \left(\frac{1}{P_c} - \frac{1}{2} + \zeta\right)\frac{\partial}{\partial\zeta} + 1\right]. \tag{4.10}$$

Finally, by substituting $T = T_b + \epsilon\mathrm{e}^{\mathrm{i}m\theta}T_1$ and $c = c_b + \epsilon\mathrm{e}^{\mathrm{i}m\theta}C_1$ into equation (2.14) and expanding in ϵ, we obtain

$$\mu \sim \mu_b + \epsilon\mathrm{e}^{\mathrm{i}m\theta}\mu_b[-\beta_T T_1 - \beta_c C_1], \tag{4.11}$$

and so

$$M_1 = -\mu_b[\beta_T T_1 + \beta_c C_1], \quad \text{i.e.} \quad N = -\mu_b[\beta_T\Theta + \beta_c\chi]. \tag{4.12}$$

Additionally, we have

$$\frac{\partial\mu_b}{\partial\zeta} = \frac{\partial\mu}{\partial T}\frac{\partial T_b}{\partial\zeta} + \frac{\partial\mu}{\partial c}\frac{\partial c_b}{\partial\zeta} = -\beta_T\mu_b\frac{\partial T_b}{\partial\zeta} - \beta_c\mu_b\frac{\partial c_b}{\partial\zeta} \tag{4.13}$$

and so, substituting these expressions into equation (4.7) and dividing through by $\mu_b(\zeta)$, we obtain

$$\frac{\partial}{\partial\zeta}\left[\zeta\frac{\partial\Upsilon}{\partial\zeta}\right] - \left(\beta_T\frac{\partial T_b}{\partial\zeta} + \beta_c\frac{\partial c_b}{\partial\zeta}\right)\left[\zeta\frac{\partial\Upsilon}{\partial\zeta}\right] = \frac{1}{4}m^2\frac{\Upsilon}{\zeta} - \frac{1}{4}m^2\frac{1}{\zeta}\left[\beta_T\Theta + \beta_c\chi\right]. \tag{4.14}$$

4.2. *Radial eigenfunctions*

We will approach the linearized problem defined above by decomposing the radial structure of the perturbations to temperature and concentration into a series of radial eigenfunctions.

A natural basis for this decomposition can be developed, following Ben *et al.* (2002) and Barenblatt (1996), by investigating the stability of the similarity solutions for T and c when there is no azimuthal flow (i.e. in the limit $m \to 0$). For convenience, we derive the eigenfunctions for the temperature perturbation first, noting that the result for the concentration perturbation will follow immediately by setting $\lambda = 1$ and $P_T = P_c$.

We consider the purely axisymmetric temperature field driven by radial injection, which is governed by the equation

$$\frac{\partial T}{\partial t} + \lambda\frac{1}{r}\frac{\partial T}{\partial r} = \frac{1}{P_T}\frac{1}{r}\frac{\partial}{\partial r}\left(r\frac{\partial T}{\partial r}\right). \tag{4.15}$$

We seek localized solutions to (4.15), which vanish at $r=0$ and as $r \to \infty$. We use the fact that if T is a solution of (4.15), so is $\partial T/\partial t$:

$$\frac{\partial T_b}{\partial t}(r,t) \propto \frac{1}{t}\mathrm{e}^{-P_T\zeta}\zeta^{\lambda P_T/2}, \tag{4.16}$$

and it is simple to verify by direct substitution that $T = \mathrm{e}^{-P_T\zeta}\zeta^{\lambda P_T/2}t^{-1}$ has the desired properties.

Adding a perturbation $\epsilon T_1 = \epsilon\partial T/\partial t$ to the basic solution T_b corresponds physically to changing the time-origin of the basic solution infinitesimally; in other words, to advancing or retarding the spreading front slightly. This is the key to the eigenfunction approach, since (following Barenblatt 1996, § 8.3) we expect such perturbations to a self-similar basic state to be neutral, whereas all other forms of perturbation will decay in time. Hence it is plausible that this eigenfunction will come to dominate the structure of the most unstable mode. (We note that this also provides a connection to the 'thin-front' approach of § 3, where the retardation or advancement of the fronts is considered explicitly.)

The form of $\partial T/\partial t$ suggests that we write (4.15) in terms of the independent variables (ζ, t) and define $T = \xi(\zeta, t)t^{-1}$. This transforms (4.15) to the equation

$$t\frac{\partial \xi}{\partial t} = \mathscr{L}_T\xi, \tag{4.17}$$

with solutions of the form $\xi_j(\zeta,t) = t^{\nu_j}\phi_j(\zeta)$ where $\phi_j(\zeta)$ satisfies the eigenfunction equation

$$\mathscr{L}_T\phi_j = \nu_j\phi_j. \tag{4.18}$$

Provided we have a suitable spectrum of eigenfunctions for the operator $\mathscr{L}_T$ with the associated boundary conditions, we can then represent any localized initial disturbance at $t=1$ in terms of these eigenfunctions, and predict its evolution by allowing them to evolve as t^{ν_j}. We note that we have already obtained one of these eigenfunctions, $\phi_0 = \mathrm{e}^{-P_T\zeta}\zeta^{\lambda P_T/2}$, which corresponds to the eigenvalue $\nu_0 = 0$.

The problem is now to obtain the remaining eigenfunctions. The form of $\phi_0(\zeta)$ suggests that we seek solutions of the form $\phi_j(\zeta) = \mathrm{e}^{-P_T\zeta}\zeta^{\lambda P_T/2}f_j(\zeta)$, which guarantees that $\phi_j(\zeta)$ will satisfy the boundary conditions as long as f_j is well-behaved at $\zeta=0$ and as $\zeta \to \infty$. Substituting this into equation (4.18), we obtain an associated Laguerre equation (Arfken & Weber 1995), and thus the eigenfunctions

$$\phi_j(\zeta) = \mathrm{e}^{-P_T\zeta}\zeta^{\lambda P_T/2}L_j^{(\lambda P_T/2)}(P_T\zeta) \quad \text{for} \quad -\nu_j = j = 0, 1, 2, \ldots \tag{4.19}$$

where $L_j^{(k)}(x)$ are the associated Laguerre polynomials.

Figure 4 shows the form of the eigenfunctions $\phi_j(\zeta)$ for two values of P_T. The function corresponding to the radial mode number j in general oscillates j times; in particular, the eigenfunction $\phi_0(\zeta)$ consists of a single 'hump' centred around the front. The typical length associated with the oscillations reduces as j increases; hence, we may expect that for large values of m the lateral perturbations force the lower radial modes more strongly, since the lateral and radial lengthscales will then be comparable. As P_T increases, the width of the front in ζ-space decreases roughly as $P_T^{-1/2}$. Consequently, the eigenfunctions for higher P_T are more strongly localized around the centre of the diffusive front.

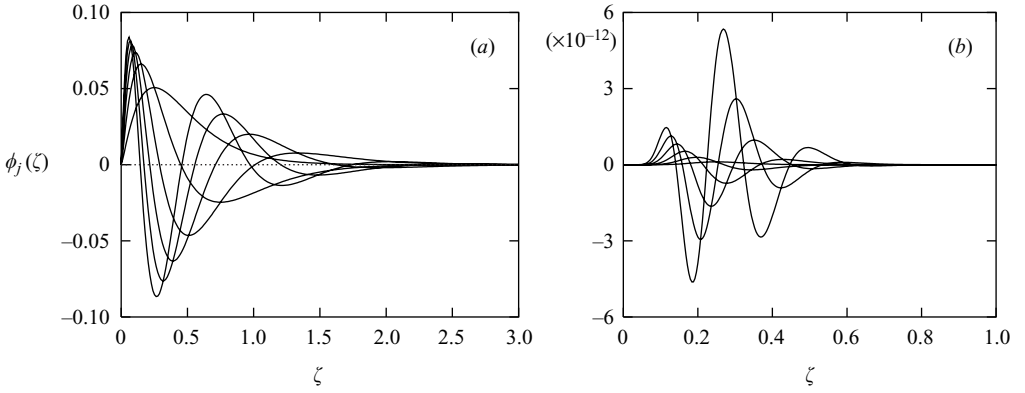

FIGURE 4. Eigenfunctions $\phi_j(\zeta)$ for $\lambda = 0.5$: (*a*) $P_T = 5$ and (*b*) $P_T = 50$, for $j = 0$ to 5.

The orthogonality relation for the set $\{\phi_j\}$ is readily obtained from that for the associated Laguerre polynomials, and is given by

$$\langle \phi_p, \phi_q \rangle_T \equiv \int_0^\infty \mathrm{e}^{P_T\zeta}\zeta^{-\lambda P_T/2}\phi_p(\zeta)\phi_q(\zeta)\,\mathrm{d}\zeta = \frac{1}{P_T^{\lambda P_T/2+1}}\frac{\Gamma\left(p+\frac{1}{2}\lambda P_T+1\right)}{\Gamma(p+1)}\delta_{p,q}, \quad (4.20)$$

where $\delta_{p,q}$ is the Kronecker delta (which we employ without invoking the summation convention). The set of eigenfunctions $\{\phi_j(\zeta)\}$ is complete with respect to sufficiently strongly localized disturbances to the temperature field, and is therefore a suitable basis for our perturbation analysis.

We have now obtained the important result that all eigenvalues of (4.18) are non-positive. This means physically that all purely radial disturbances to the temperature field must decay: the solution is therefore linearly stable to instantaneously imposed, axisymmetric perturbations. The least strongly decaying mode, $\phi_0(\zeta)$, represents an infinitesimal change of the time-origin of the basic solution; in other words, to infinitesimally advancing or retarding the position of the front. This will be of importance later in interpreting the radial structure of unstable (non-axisymmetric) perturbations.

Carrying out the corresponding analysis for the solute concentration field, we obtain the eigenfunction equation $\mathscr{L}_c\psi_j = \nu_j\psi_j$, and hence the spectrum of eigenfunctions

$$\psi_j(\zeta) = \mathrm{e}^{-P_c\zeta}\zeta^{P_c/2}L_j^{(P_c/2)}(P_c\zeta), \qquad \text{where} \quad j = 0, 1, 2, \ldots \quad (4.21)$$

with the orthogonality relation

$$\langle \psi_p, \psi_q \rangle_c \equiv \int_0^\infty \mathrm{e}^{P_c\zeta}\zeta^{-P_c/2}\psi_p(\zeta)\psi_q(\zeta)\,\mathrm{d}\zeta = \frac{1}{P_c^{P_c/2+1}}\frac{\Gamma\left(p+\frac{1}{2}P_c+1\right)}{\Gamma(p+1)}\delta_{p,q}. \quad (4.22)$$

Finally, for numerical convenience, we define rescaled eigenfunctions

$$\Phi_p(\zeta) = G_p\phi_p(\zeta), \quad \Psi_q(\zeta) = H_q\psi_q(\zeta), \quad (4.23)$$

where an appropriate choice of the prefactors G_p and H_q (see Appendix B) allows us to avoid the computational problems caused by the rapid decay of ϕ_p and ψ_q with increasing Péclet numbers and eigenmode numbers. (Note that different rescalings were used for different ranges of the Péclet numbers: the effect of this rescaling is apparent in the amplitude of the perturbations plotted in § 5.)

4.3. *Setting up the eigenvalue problem*

4.3.1. *Radial decomposition*

For a given value of the azimuthal wavenumber m, we decompose the radial structure of the temperature and solute perturbations in terms of the appropriate eigenfunctions,

$$\Theta(\zeta,t)=\sum_{p=0}^{\infty}A_p^T(t;m)\Phi_p(\zeta),\quad \chi(\zeta,t)=\sum_{q=0}^{\infty}A_q^c(t;m)\Psi_q(\zeta). \tag{4.24}$$

We now exploit the linearity of equation (4.14) and write

$$\Upsilon(\zeta,t)=\sum_{p=0}^{\infty}A_p^T(t;m)\varpi_p^T(\zeta)+\sum_{q=0}^{\infty}A_q^c(t;m)\varpi_q^c(\zeta), \tag{4.25}$$

where $\varpi_p^T(\zeta)$ and $\varpi_q^c(\zeta)$ satisfy the equations

$$\left(\frac{\partial}{\partial\zeta}\left[\zeta\frac{\partial}{\partial\zeta}\right]-\left[\beta_T\frac{\partial T_b}{\partial\zeta}+\beta_c\frac{\partial c_b}{\partial\zeta}\right]\left[\zeta\frac{\partial}{\partial\zeta}\right]-\frac{1}{4}\frac{m^2}{\zeta}\right)\left\{\begin{array}{c}\varpi_p^T\\ \varpi_q^c\end{array}\right\}=\frac{1}{4}\frac{m^2}{\zeta}\left\{\begin{array}{c}\beta_T\Phi_p\\ \beta_c\Psi_q\end{array}\right\}, \tag{4.26}$$

both subject to the boundary conditions $\varpi_{p,q}^{T,c}(0)=0$ and $\varpi_{p,q}^{T,c}(\zeta)\to 0$ as $\zeta\to\infty$. These equations were integrated numerically to obtain $\varpi_{p,q}^{T,c}(\zeta)$: details are given in Appendix B.

4.3.2. *Amplitude evolution equations*

We construct evolution equations for the amplitudes $A_p^T(t)$ and $A_q^c(t)$ by taking the inner products $\langle\cdot,\cdot\rangle_T$ and $\langle\cdot,\cdot\rangle_c$ of equations (4.8) and (4.9) with the radial eigenfunctions $\Phi_j(\zeta)$ and $\Psi_j(\zeta)$ respectively. We obtain the coupled amplitude evolution equations

$$t\frac{\mathrm{d}A_j^T}{\mathrm{d}t}=\sum_{p=0}^{\infty}Q_{j,p}^{TT}A_p^T+\sum_{p=0}^{\infty}Q_{j,p}^{Tc}A_p^c,\quad t\frac{\mathrm{d}A_j^c}{\mathrm{d}t}=\sum_{p=0}^{\infty}Q_{j,p}^{cT}A_p^T+\sum_{p=0}^{\infty}Q_{j,p}^{cc}A_p^c, \tag{4.27}$$

where the coefficients $Q_{j,p}^{kl}$, where $k,l=T$ or c, are given by equations (C 22) to (C 25), and the details of the construction are described in Appendix C.

Finally, we write this linear system as a single matrix equation. Defining

$$B_r(t)=\begin{cases}A_{r/2}^T & \text{for}\quad r\quad\text{even},\\ A_{(r-1)/2}^c & \text{for}\quad r\quad\text{odd},\end{cases} \tag{4.28}$$

we can write the evolution equations as

$$t\frac{\mathrm{d}B_r}{\mathrm{d}t}=\sum_{s=0}^{\infty}R_{r,s}B_s\quad\text{for}\quad R_{r,s}=\begin{cases}Q_{j,p}^{TT} & \text{for}\quad r=2j\quad\text{and}\quad s=2p,\\ Q_{j,p}^{Tc} & \text{for}\quad r=2j\quad\text{and}\quad s=2p+1,\\ Q_{j,p}^{cT} & \text{for}\quad r=2j+1\quad\text{and}\quad s=2p,\\ Q_{j,p}^{cc} & \text{for}\quad r=2j+1\quad\text{and}\quad s=2p+1,\end{cases} \tag{4.29}$$

where $j,p\in\mathbb{N}$ in each case.

The eigenvalues ν of the matrix $\boldsymbol{R}\equiv R_{r,s}$ then provide the growth rates t^{ν} of successive modes, while the corresponding eigenfunctions supply the structures of the corresponding radial perturbations. Because of the factor of t^{-1} which was introduced in the definitions of Θ, χ and Υ, and the distinction between perturbations in r and

in ζ, the eigenvalues ν are related to the growth rates ω defined in § 3 by $\omega = \nu - \frac{1}{2}$. Instability in the sense of Tan & Homsy (1987) therefore corresponds to $\nu > 1$, while instability in the sense of a growing perturbation to the r-position of the 'middle' of each front corresponds to $\nu > \frac{1}{2}$.

In principle, $\boldsymbol{R}$ is a matrix of infinite rank. In practice, we calculate an approximation $\boldsymbol{R}_N$ of rank $2N+2$ by considering only the eigenfunctions Φ_0 to Φ_N and Ψ_0 to Ψ_N. (The quantity N was typically taken to be between 5 and 10: we find that the structure of the more rapidly growing modes is dominated strongly by the lowest radial eigenfunctions, and so the approximation is good. For brevity, detailed verification of this point is omitted below.)

5. Results

We now discuss the results of the stability analysis for a variety of interesting cases. We first briefly consider cases when the viscosity depends only on the temperature or only on the composition of the fluid, and our results are comparable to those of Tan & Homsy (1987). We then investigate what happens when both fronts are unstable or when one front is unstable and the other is stable.

5.1. *Values of parameters*

In principle, the only restriction on the Péclet numbers is that the ratio $P_c/P_T \gg 1$: any absolute value of P_c or P_T can be attained by varying the injection rate $\hat{Q}$. For computational convenience, we will concentrate on cases where $P_c \leqslant 1000$ and P_c/P_T is between 20 and 100. Our results suggest that this difference in the diffusivities is sufficient to reveal the physical structure of the problem; it also accords with the solutions for reacting fronts presented by Jupp & Woods (2003), which employed $P_c/P_T = 20$.

We need also consider only a fairly narrow range of β_T and β_c, since the mobility ratio is an exponential function of β_T and β_c. We consider values in the range $|\beta_{T,c}| \leqslant 10$, which are comparable to those considered in previous studies.

The porosities of porous media may vary considerably, as may their specific heat capacities. Typical porosities for natural rocks range between 0.1 and 0.4, though they may be somewhat higher or lower than this, while the specific heat capacities of many common rocks are of the order of $800\,\mathrm{J\,kg^{-1}\,K^{-1}}$ (Bear 1972), and their solid density is of the order of $2600\,\mathrm{kg\,m^{-3}}$. The specific heat capacity and density of fresh water are approximately $4200\,\mathrm{J\,kg^{-1}\,K^{-1}}$ and $1000\,\mathrm{kg\,m^{-3}}$, while the equivalent values for mineral oil are around $2000\,\mathrm{J\,kg^{-1}\,K^{-1}}$ and 800–$1000\,\mathrm{kg\,m^{-3}}$ (Somerton 1992). Taking these values together gives typical values of λ in the range 0.08 to 0.6; to elucidate the effect of strong coupling, we will occasionally consider values rather higher than this.

5.2. *One unstable and one neutral front*

5.2.1. *Fluid front unstable; thermal front neutral*

We first consider briefly the case in which the fluid front is unstable, $\beta_c < 0$, and the thermal front is neutral, $\beta_T = 0$. The structure of the eigenvalue spectrum is illustrated in figure 5(a), and the radial structure of the perturbations is illustrated in figure 5(b, c): both of these are representative of conditions across a wide range of parameter values.

We first consider the eigenvalues (figure 5a). The eigenvalue spectrum is discrete, in contrast to those typically found by applying a quasi-steady theory to rectilinear

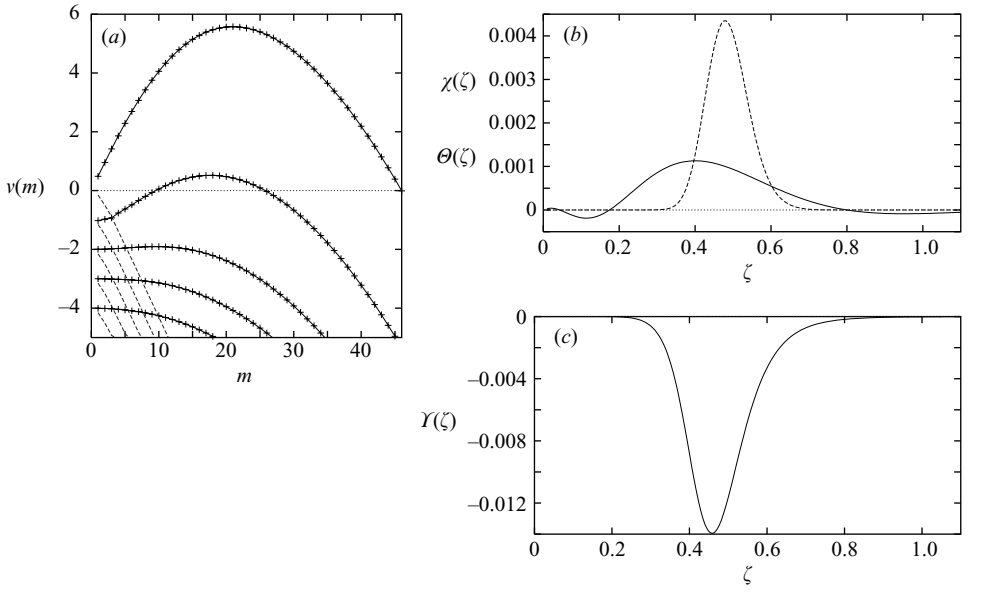

FIGURE 5. Illustrative eigenvalue spectrum and radial structure of fastest-growing perturbations for $m = m_{\max}$ when fluid front is unstable and thermal front is neutral: $\beta_c = -5$, $\beta_T = 0$, $P_T = 5$, $P_c = 100$, $\lambda = 0.6$. (*a*) Eigenvalues $\nu_j^+(m)$ corresponding to $\chi \neq 0$ modes (solid with + symbols) and $\nu_j^-(m)$ corresponding to $\chi = 0$ modes (dashed); (*b*) thermal and solute perturbations $\Theta(\zeta)$ (solid; exaggerated by factor of 30), $\chi(\zeta)$ (dashed); (*c*) flux perturbation $\Upsilon(\zeta)$.

displacements (Manickam & Homsy 1993), and eigenvalues occur in pairs $\nu_j^{\pm}(m)$, which reduce as $m \to 0$ to the eigenvalues of $\mathscr{L}_c$, $\nu_j = -j$ (see §4.2). The highest eigenvalue is $\nu_0^+(m)$, which reduces to $\nu_0 = 0$ at $m = 0$, and the results for this eigenvalue agree well with the data presented by Tan & Homsy (1987). In each pair of eigenvalues, ν_j^+ corresponds to an eigenvector for which $\chi \neq 0$, while ν_j^- corresponds to an eigenvector for which $\chi = 0$, and represents the decay of the temperature perturbation under passive diffusion and the spreading of the front.

Tan & Homsy's analysis was designed to capture only one eigenvalue for a given set of parameters, and so it did not reveal the behaviour of the higher radial modes. An interesting feature which the eigenfunction analysis reveals is that for sufficiently high values of P_c and $-\beta_c$, a second radial mode $\nu_1^+(m)$ also becomes unstable, with a preferred wavenumber slightly lower than that of the most unstable mode. In the weakly nonlinear regime this second growing mode might interact with the most unstable mode to produce effects such as the spreading and tip-splitting of fingers (q.v. the analysis for immiscible Hele-Shaw flow by Miranda & Widom 1998); however, this lies beyond the scope of the current study.

The most striking feature of the structure of the fastest-growing perturbation (figure 5*b*, *c*) is that both the solute perturbation $\chi(\zeta)$ and the thermal perturbation $\Theta(\zeta)$ are dominated by the zero-eigenfunctions ($\Psi_0(\zeta)$ and $\Phi_0(\zeta)$ respectively). Consequently, the solute perturbation is a single 'hump' centred on $\zeta = 1/2$, while the thermal perturbation is a rather wider hump centred approximately on $\zeta = \lambda/2$. The structure of the velocity perturbation $\Upsilon(\zeta)$ (figure 5*c*) is also dominated by a single extremum, but decays more slowly away from the front position, especially outwards

from it, reflecting its algebraic asymptotic behaviour in ζ as opposed to the exponential decay of $\Theta(\zeta)$ and $\chi(\zeta)$.

The dominance of $\Psi_0(\zeta)$ in $\chi(\zeta)$ reflects the structure of the eigenvalue spectrum. In the limit $m \to 0$, each eigenvalue pair $\nu_j^{\pm}(m)$ reduces to $\nu_j = -j$, and the corresponding eigenfunctions similarly reduce to $\chi(\zeta) = \Psi_j(\zeta)$, as in §4.2. This eigenfunction continues to dominate the structure of the perturbation for higher m, although as m increases so does the presence of other components Ψ_j.

However, the temperature perturbation $\Theta(\zeta)$ plays no part in the stability of the front, and so the dynamical explanation given above for $\chi(\zeta)$ cannot apply to it. Rather, $\Phi_0(\zeta)$ dominates the passive temperature perturbation for two reasons. First, because the zero eigenfunction varies least rapidly in space, it is reduced least by radial diffusion. The second mechanism is best understood by considering the dynamics along the centreline of a 'finger', $\theta = 0$. The perturbation to radial velocity has a single extremum in the region of the fluid front, and so it is locally slowly-varying in the region of the thermal front. Consequently, its effect is, to leading order, to slightly increase or decrease flow in this region, and thus to slightly advance or retard the position of the thermal front. As we have seen, such an advance or retardation corresponds to perturbing the basic state $T_b(\zeta)$ by an amount proportional to $\Phi_0(\zeta)$. Since these arguments apply in general to the front perturbations, we find that in general the zero eigenfunctions dominate the structure of the fastest-growing perturbations.

A second feature of figure 5(*b*) is that the solute perturbation is very much larger than the thermal perturbation. This occurs primarily because it is much less affected by diffusion, but also because the forcing induced by the velocity perturbation Υ is rather weak at the position of the thermal front. A parameter study varying λ and P_T (omitted here for brevity) suggests that these effects are comparable in magnitude.

5.2.2. *Thermal front unstable; fluid front neutral*

We also consider briefly the case where the instability occurs on the thermal front and there is no viscosity change across the fluid front. This is illustrated in figure 6.

Where the instability is controlled only by the diffusing thermal front, we may obtain the eigenvalues immediately from the analysis of the diffusing solute front by rescaling. The crucial rescalings are to define a new time variable $t' = \lambda^{-1}t$ and to set $P_c = \lambda P_T$: the rescaled equation (2.6) then becomes identical to the original equation (2.7), and so the highest eigenvalues ν are the same in the two cases. Following this rescaling, our results for the highest eigenvalue again compare well with those of Tan & Homsy (1987).

The structure of the eigenvalue spectrum (figure 6*a*) is similar to that for the fluid-front instability, with pairs of eigenvalues $\nu_j^{\pm}(m)$ and a single most-unstable mode $\nu_0^{+}(m)$. We have this time denoted by $\nu_j^{+}(m)$ the eigenvalue branches for which $\Theta \neq 0$ and by $\nu_j^{-}(m)$ the branches for which $\Theta = 0$ and the growth rate represents the passive diffusion of solute. This introduces a slight notational anomaly, which is that because $P_c \gg P_T$ the $\Theta = 0$ eigenvalues are higher than those which include a temperature perturbation, except for the range of m in which the dynamic instability on the front is able to overcome diffusion.

The structures of both thermal and solute perturbations (figure 6*b*) are again dominated by the zero-eigenfunctions $\Psi_0(\zeta)$ and $\Phi_0(\zeta)$, and the flux perturbation $\Upsilon(\zeta)$ (figure 6*c*) has its maximum slightly inwards of the unstable front; because of the lower value of $m_{\max}$ than in the previous case, the decay of $\Upsilon(\zeta)$ away from the front is rather slower than in figure 5.

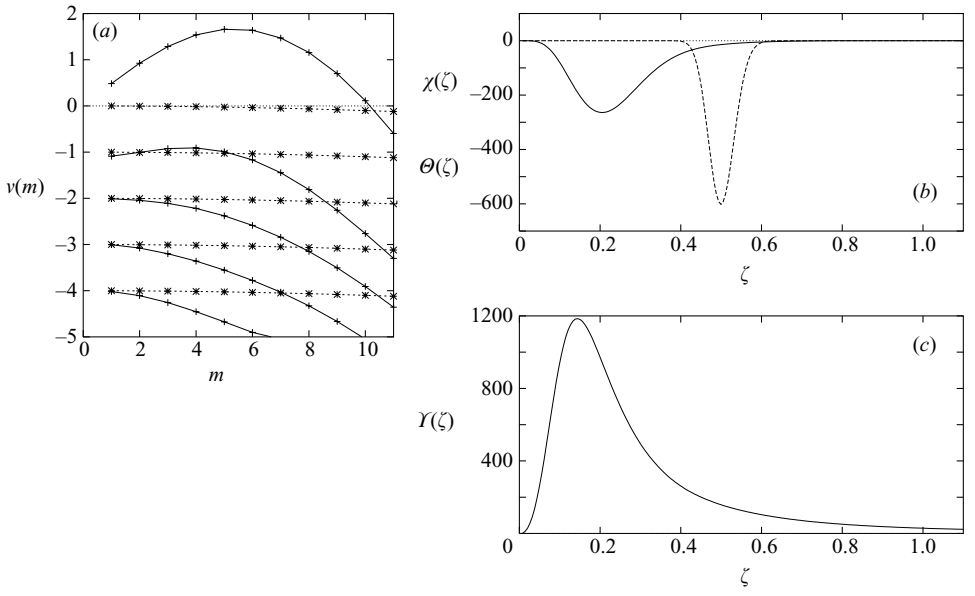

FIGURE 6. Illustrative eigenvalue spectrum and radial structure of fastest-growing perturbations for $m = m_{\max}$ when thermal front is unstable and fluid front is neutral: $\beta_c = 0$, $\beta_T = -10$, $P_T = 20$, $P_c = 500$, $\lambda = 0.5$. (*a*) Eigenvalues $v_j^+(m)$ corresponding to $\Theta \neq 0$ modes (solid with + symbols) and $v_j^-(m)$ corresponding to $\Theta = 0$ modes (dashed with stars); (*b*) thermal and solute perturbations $\Theta(\zeta)$ (solid) and $\chi(\zeta)$ (dashed); (*c*) flux perturbation $\Upsilon(\zeta)$.

5.3. *Two fronts*

We now consider the more general cases in which the viscosity changes across both the fluid front and the thermal front.

When both fronts are unstable, the greater fluid Péclet number means that the instability on the fluid front is suppressed much less by diffusion than that on the thermal front, and so the overall instability comes to be controlled by the fluid front. In § 5.3.1, we investigate how much the instability or stability of the thermal front affects the perturbations. When the thermal front is unstable but the fluid front is stable, on the other hand, there is the opportunity for a rather complicated interaction between the highly localized solute perturbation and the more diffuse thermal perturbation: we consider this in § 5.3.2.

5.3.1. *Fluid front unstable; thermal front stable or unstable*

The extent to which the thermal front can modify the stability of the system is illustrated in figure 7, which shows the highest eigenvalues for $\beta_c = -1$ and a range of values of β_T, for three values of λ. As λ increases, the velocity perturbation associated with each front 'sees' more of the viscosity contrast associated with the other front, and so the dynamics become more strongly coupled. This shows up in the much greater spread of the eigenvalues plotted for $\lambda = 0.75$ (figure 7*c*) compared to those for $\lambda = 0.25$ (figure 7*a*).

In general, the effect of the thermal front is only to modify slightly the stability of the system, which is principally determined by the fluid front. In particular, an unstable thermal front can enhance the growth rates of the most unstable perturbations substantially at low m, and a stable thermal front generally reduces growth rates, again particularly at low m. As m increases, the perturbations become more strongly

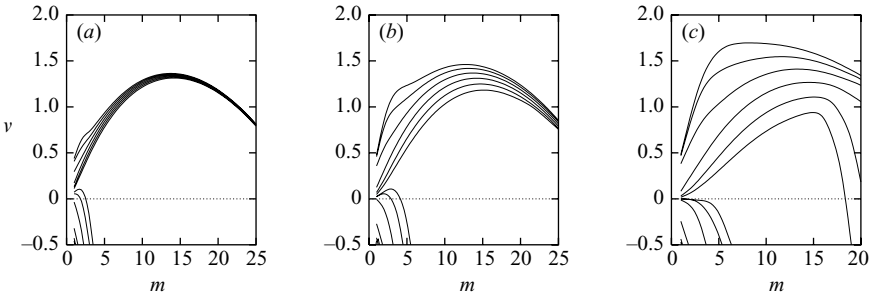

FIGURE 7. Eigenvalues $\nu_0^{\pm}(m)$ of $\boldsymbol{R}_5$ for the parameter values $P_c = 200$, $P_T = 10$, $\beta_c = -1$, $\beta_T = -10$ to 10 and (*a*) $\lambda = 0.25$; (*b*) $\lambda = 0.5$; (*c*) $\lambda = 0.75$. In each case, the highest values of ν correspond to $\beta_T = -10$ and the lowest to $\beta_T = 10$. The lines joining successive values of m are to guide the eye.

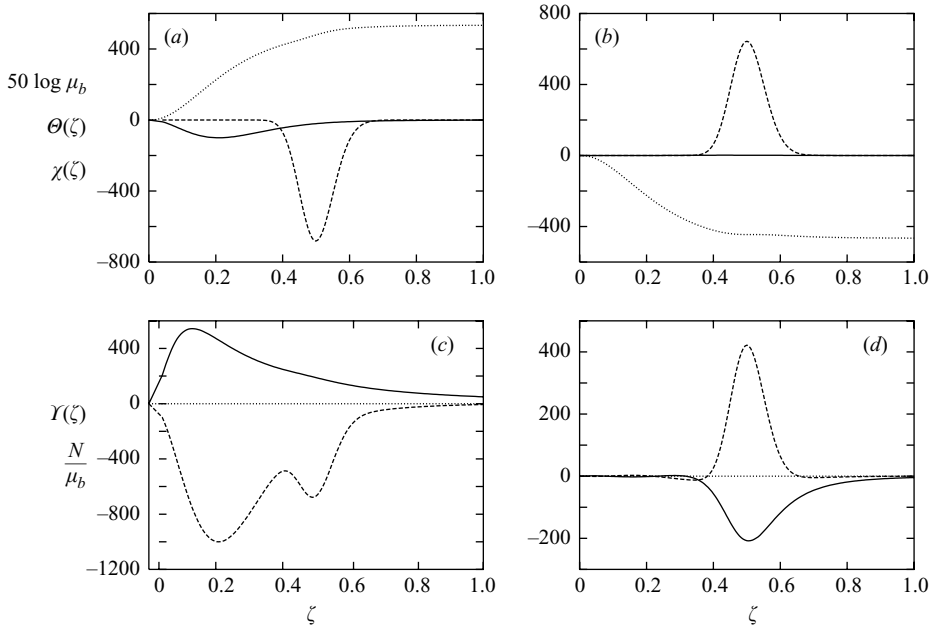

FIGURE 8. Radial structure of perturbations for $P_c = 200$, $P_T = 10$, $\beta_c = -0.68$, $\lambda = 0.5$: (*a*) $\beta_T = -10$ and $m = 4$ ($\nu_0^+ = 1.06$); (*b*) $\beta_T = 10$ and $m = 13$ ($\nu_0^+ = 0.64$). In the upper plots, solid lines represent $\Theta(\zeta)$, dashed lines represent $\chi(\zeta)$ and dotted lines represent the background viscosity profile (the quantity plotted is $50 \log \mu_b(\zeta)$ for visual convenience). In the lower plots, solid lines represent $\Upsilon(\zeta)$ and dashed lines represent $N(\zeta)/\mu_b(\zeta)$.

localized (cf. § 3), so the thermal front exerts less influence on the fluid front, and this shows in the convergence of the eigenvalues for different values of β_T.

At very high values of λ, it is possible for a strongly stable thermal front to reduce the instability of the fluid front substantially (figure 7*c*). It is interesting that even though the stabilization is most marked for high values of m, the strong coupling at low wavenumbers tends to increase the most unstable wavenumber, leading to rather a sharp cut-off for $m > m_{\max}$. This is discussed further below.

To illustrate the coupling process, figure 8 shows the fastest-growing perturbations for a slightly unstable fluid front ($\beta_c = -0.68$) when $\lambda = 0.5$, both when the thermal front is strongly unstable and when it is strongly stable.

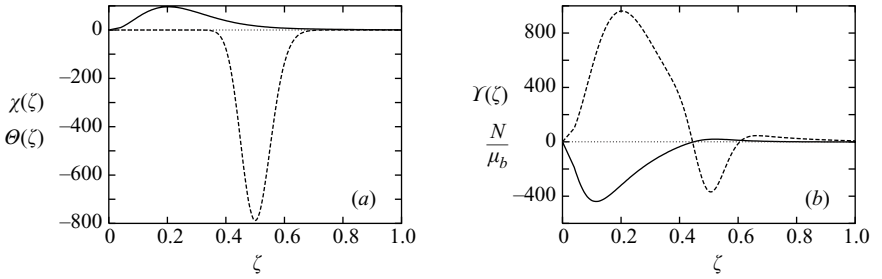

FIGURE 9. Radial structure of ν_0^- perturbation for $P_c = 200$, $P_T = 10$, $\beta_c = -0.68$, $\beta_T = -10$, $\lambda = 0.5$ and $m = 4$ ($\nu_0^- = 0.011$). In (*a*), solid lines represent $\Theta(\zeta)$ and dashed lines represent $\chi(\zeta)$; in (*b*), solid lines represent $\Upsilon(\zeta)$ and dashed lines represent $N(\zeta)/\mu_b(\zeta)$.

When the fluid front is weakly unstable and the thermal front is strongly unstable (figure 8*a*), the overall instability of the system is enhanced, and the most unstable wavenumber may be substantially reduced. (For high P_c and P_T and small β_T and β_c, separate local maxima may occur corresponding to instabilities localized around each front, but the two maxima merge smoothly as the degree of instability increases.) Because of the higher solute Péclet number, the solute perturbation $\chi(\zeta)$ is rather larger than the thermal perturbation $\Theta(\zeta)$; however, because $|\beta_T|$ is substantially larger than $|\beta_c|$, both perturbations contribute significantly to the perturbation to viscosity, and hence to the velocity perturbation. Consequently, there is quite a wide region (from the innermost point of the thermal front to the outermost of the fluid front) in which velocity and viscosity are perturbed.

The fastest-growing branch of perturbations, which correspond to the eigenvalues $\nu_0^+(m)$, are sinuous in character, with both Θ and $\chi > 0$, indicating that both fronts have been infinitesimally retarded. Recalling the 'thin-front' results of Cardoso & Woods (1995) and of § 3, it is interesting also to consider briefly the secondary branch which corresponds to $\nu_0^-(m)$. We expect this to be varicose in character, and figure 9 indicates that this is the case. On this branch, the perturbations to temperature and viscosity have opposite signs. They therefore induce opposing perturbations to viscosity, and so the fluid front acts as a barrier to the velocity perturbation induced by the thermal front, causing it to be strongly localized. The competition between the frontal perturbations explains the strong decay of this branch of the perturbations. Comparing the analysis of § 3, we note that because diffusion allows much stronger communication between the perturbations on the two fronts, it weakens the varicose mode much more strongly compared to the 'thin-front' case than it does the sinuous mode in which the perturbations assist each other.

When the fluid front is weakly unstable but the thermal front is strongly stable (figure 8*b*), the overall viscosity profile may favour stability: in this case, the basic viscosity profile decreases monotonically outwards even across the fluid front. However, an instability occurs which is strongly localized around the fluid front and so barely perturbs the temperature field. In the region of this instability, a positive velocity perturbation 'pulls forward' both the thermal and the solute components of the viscosity field; since the solute component is advected more strongly than the thermal by a factor λ^{-1}, and is reduced less in magnitude by diffusion, the net perturbation in the viscosity field at the fluid front is negative, and instability occurs. Thus, even though the overall background viscosity profile appears stable, the different rates of heat and fluid transport allow the development of a localized instability. This

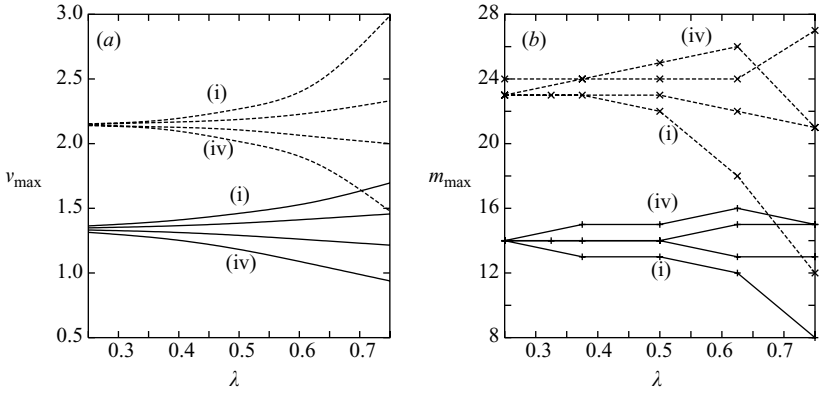

FIGURE 10. (*a*) Maximum eigenvalue v_{max} and (*b*) the corresponding azimuthal wavenumber m_{max} for $\beta_c = -1$. Solid lines represent $P_c = 200$ and $P_T = 10$; dashed lines represent $P_c = 400$ and $P_T = 20$. Numbers label the solutions corresponding to various values of β_T: (i) $\beta_T = -10$; (ii) $\beta_T = -\frac{10}{3}$; (iii) $\beta_T = \frac{10}{3}$; (iv) $\beta_T = 10$. Where lines are not numbered the values of β_T can be inferred by interpolation.

instability of an apparently stable viscosity profile complements the effect noted by Manickam & Homsy (1993) for a non-monotonic $\mu(c)$ relationship, when a localized instability can develop from a non-monotonic viscosity profile even though the global viscosity contrast across the front is stable. It is also analagous to the instability of an apparently statically stable density profile in double-diffusive convection (see Turner 1979, chap. 8).

As figure 7(*c*) illustrates, it is extremely difficult to stabilize this fluid-front instability completely, even for high values of λ. However, because it is strongly localized it is vulnerable to diffusion at high m; combined with the dynamic stabilization through the velocity perturbation at low m, this narrows the window of unstable wavenumbers considerably as λ and β_T increase.

The difference in stability is illustrated in figure 10, which shows the variation in v_{max} and m_{max} for two different values of P_c, as λ and β_T are varied keeping the fluid front viscosity contrast β_c and the ratio P_c/P_T fixed.

These plots illustrate the essential role of λ in controlling the coupling between the fronts. The relative change in the range of maximum eigenvalues is roughly the same for $\lambda = 0.75$ for both cases considered, but especially for the higher Péclet numbers (for which the perturbations are more strongly localized) the variation only becomes significant for $\lambda \gtrsim 0.5$. This suggests that in most porous rocks, it is difficult for temperature variations to stabilize significantly a slightly unstable fluid front. (The stabilizing effect of the thermal front also decreases as the ratio P_c/P_T increases, increasing the relative effect of diffusion on the thermal front and thus weakening its ability to affect the fluid front.)

Overall, the variation in m_{max} is not great, with the preferred wavenumber remaining within 1 or 2 of its value for the isolated fluid front. The exception occurs when β_T is large and negative, when the preferred wavenumber which is obtained becomes a compromise between the preferred scales of the thermal and fluid front instabilities.

5.3.2. *Thermal front unstable; fluid front stable*

The final case which we will consider occurs when the fluid front is stable, $\beta_c > 0$, and the thermal front is unstable, $\beta_T < 0$. In this case, the stable fluid front may act

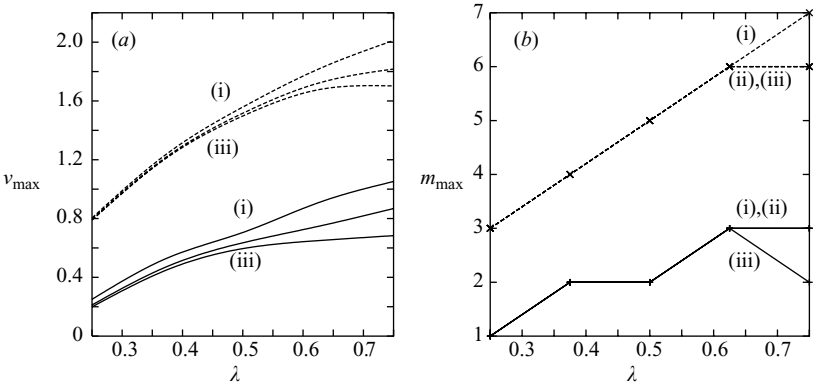

FIGURE 11. (*a*) Maximum eigenvalue $v_{\max}$ and (*b*) the corresponding azimuthal wavenumber $m_{\max}$ for $\beta_T = -10$. Solid lines represent $P_c = 200$ and $P_T = 10$; dashed lines represent $P_c = 400$ and $P_T = 20$. Numbers label the solutions corresponding to various values of β_c: (i) $\beta_c = 1$; (ii) $\beta_c = 2$; (iii) $\beta_c = 3$. Where lines are not numbered the values of β_c can be inferred by interpolation.

as a barrier to the perturbation induced on the unstable thermal front, in the same way as for the varicose mode of § 5.3.1 (figure 9*b*). The dynamics are rather different from those which occur when a stable thermal front affects an unstable fluid front, because the stabilizing influence is now strongly localized.

Figure 11 illustrates the extent to which the fluid front can stabilize the thermal front for two values of P_T. (We found that the ratio P_c/P_T was not important in this case, once it became large enough that the fluid front was much narrower than the thermal front.)

The trend is not quite so clear as before, partly because the growth rate and preferred wavenumber of the thermal front even for $\beta_c = 0$ increase with λ (we recall that the crucial quantity in this case is λP_T). However, the effect of the fluid front in stabilizing the thermal front is evident, particularly for higher values of λ. This trend too is slightly weaker, because the more diffuse thermal perturbation naturally 'sees' obstacles further away than the fluid perturbation did. As before, the dependence of the growth rate on λ is more marked for higher Péclet numbers P_T.

Figure 12 illustrates the eigenvalue spectrum for two of the cases shown in figure 11. The overall structure is similar to the cases considered previously, but there is a new feature, which is that some of the eigenvalues are now complex, $v = v_r + \mathrm{i}v_i$. These complex eigenvalues are formed when two adjacent eigenvalues coalesce to form a complex-conjugate pair with correspondingly complex-conjugate eigenfunctions: the pair which merge may be the upper and lower parts of one branch, as in the merger of $v_0^{\pm}(m)$ at $m = 5$ in figure 12(*a*), or they may belong to different branches, as in the merger of $v_0^{-}(m)$ and $v_1^{+}(m)$ at $m = 4$ in figure 12(*b*).

In general, the formation of complex eigenvalues appears to be more common on the lower eigenvalue branches than on the uppermost branch $v_0^{\pm}(m)$, and when it does occur on the uppermost branch this tends to be for values of $m > m_{\max}$. Cases for which $\mathrm{Im}(v_{\max}) \neq 0$ occur only at the limits of the parameter range considered here, when the growth of the instability is sufficiently suppressed that $m_{\max} = 1$. For example, for $\lambda = 0.75$, $\beta_T = -10$, $\beta_c = 2$, $P_T = 3$ and $P_c = 50$, we find $m_{\max} = 1$ with $v_r = 0.144$ and $v_i = 0.072$.

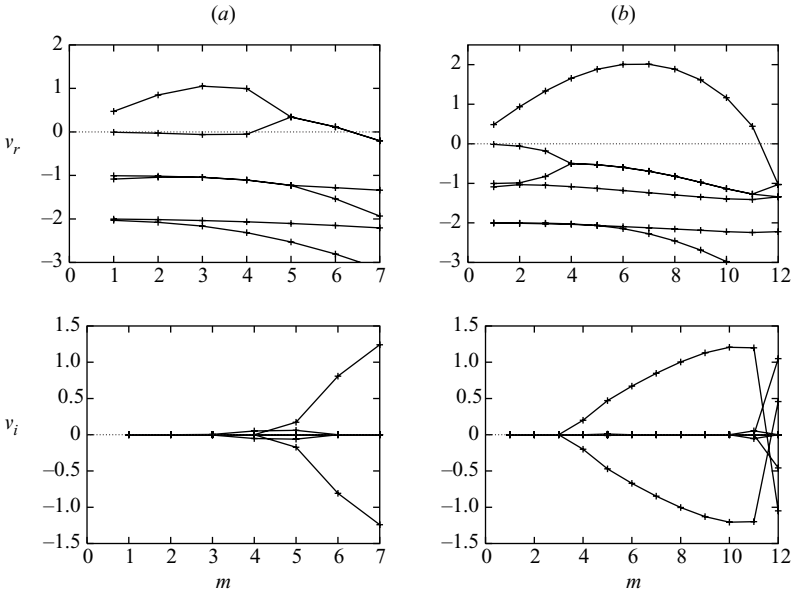

FIGURE 12. Real and imaginary parts of eigenvalues $\nu(m)$ for $\beta_T = -10$, $\beta_c = 1$, $\lambda = 0.75$: (*a*) $P_c = 200$, $P_T = 10$; (*b*) $P_c = 400$, $P_T = 20$.

Although this phenomenon is not likely to dominate the observed instability in most physically realizable cases, there are at least two reasons for seeking to understand it. First, as figure 12 a illustrates, the coalescence of the eigenvalues as m increases is associated with a sharp drop in ν_0^+, and therefore the physical mechanism represented by the complex eigenvalues plays an important part in stabilizing the perturbation at values of m slightly above $m_{\max}$, and thus in determining $m_{\max}$ itself. Second, since in at least some cases the complex eigenvalues have positive real parts, they may be physically relevant to the nonlinear development of the instability. (We recall that since growth rates are algebraic in t, the difference in magnitude between the growing modes is likely to be established rather slowly.) We now therefore consider the phenomenon in some detail.

Physically, the presence of complex eigenvalues $\nu_\pm = \nu_r \pm \mathrm{i}\nu_i$ means that the instability has an oscillatory character. If we define the corresponding eigenvectors $\boldsymbol{B}_\pm = \boldsymbol{B}_r \pm \mathrm{i}\boldsymbol{B}_i$, then we can write the evolution equations for these two modes as

$$t\frac{\mathrm{d}}{\mathrm{d}t}\begin{pmatrix}\boldsymbol{B}_r\\ \boldsymbol{B}_i\end{pmatrix} = \begin{pmatrix}\nu_r & \nu_i\\ -\nu_i & \nu_r\end{pmatrix}\begin{pmatrix}\boldsymbol{B}_r\\ \boldsymbol{B}_i\end{pmatrix}. \tag{5.1}$$

For oscillatory growth to occur, $\nu_r > 0$, the imaginary component must encourage its own growth as well as that of the real component, while the real component encourages its own growth but tends to suppress that of the imaginary component.

We can then write the evolving physical part of the perturbation $\boldsymbol{B}$ as

$$\mathrm{Re}(\boldsymbol{B}\mathrm{e}^{\mathrm{i}m\theta}) = B_0 t^{\nu_r}\cos(m\theta)\left[\boldsymbol{B}_r(\zeta)\cos(\tau) - \boldsymbol{B}_i(\zeta)\sin(\tau)\right], \tag{5.2}$$

where B_0 is an initial amplitude, $\tau \equiv \varphi + \nu_i \log t$ is the 'phase time' of the oscillation, and φ is a phase angle which represents the relative magnitudes of the $\boldsymbol{B}_r$ and $\boldsymbol{B}_i$ components at time $t = 1$. The fingers are stationary in the azimuthal direction,

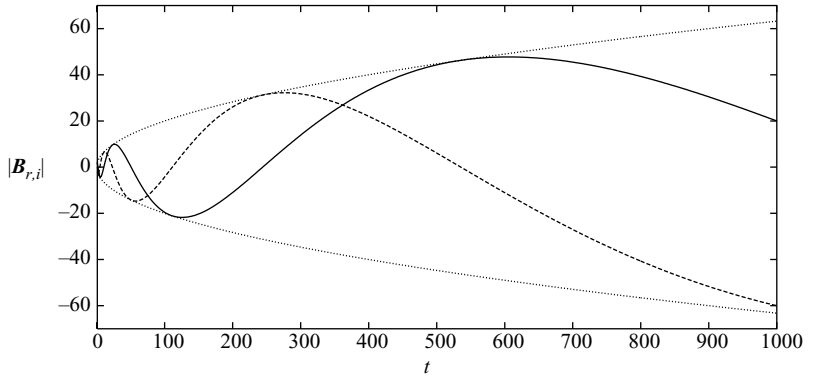

FIGURE 13. Relative amplitudes of the real (solid) and imaginary (dashed) components of $\boldsymbol{B}$ for $\nu_r = 0.5$, $\nu_i = 2$, contrasted with $\pm t^{\nu_r}$ (dotted).

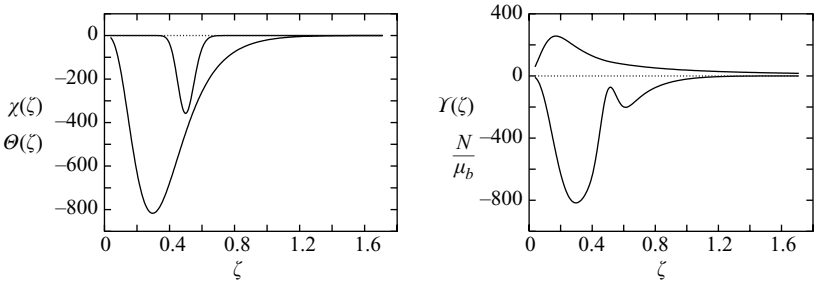

FIGURE 14. Radial structure of fastest-growing perturbations for $P_c = 200$, $P_T = 10$, $\beta_c = 1$, $\beta_T = -10$, $\lambda = 0.75$ and $m = 3$ ($\nu = 1.052$). Temperature perturbation $\Theta(\zeta)$ is exaggerated by a factor of 10 for clarity.

with 'positive' fingers centred on $\theta = 2n\pi/m$ ($n \in \mathbb{Z}$) and 'negative' fingers at $\theta = (2n + 1)\pi/m$, and the 'envelope' of maximum finger amplitude grows as t^{ν_r}; superimposed on this algebraic growth is an oscillatory component, represented by the term $\cos(\tau)$. The oscillation of the $\boldsymbol{B}_i$ component leads that of the $\boldsymbol{B}_r$ component by $\pi/2$. This is illustrated in figure 13.

A consequence of the oscillation is that for most of the time, the amplitude of the perturbation is lower than the purely algebraic growth rate t^{ν_r} would suggest (figure 13). However, the growth rate $\mathrm{d}|\boldsymbol{B}|/\mathrm{d}t$ may be lower or higher.

We now consider the radial structure of the perturbations. Figure 14 shows the structure of the most unstable mode ($m = 3$), and figure 15 a shows the corresponding structure of the first complex mode ($m = 5$) at $\tau = 0$, for the case plotted in figure 12(a). The structure of the most unstable perturbation is sinuous, with the temperature perturbation effect controlling the viscosity perturbation except in a small region around the fluid front, where the sudden increase in viscosity produces a barrier to the velocity perturbation. Consequently the velocity perturbation is limited in extent and in magnitude, and so the fluid front stabilizes the thermal front.

The first complex mode is also sinuous at $\tau = 0$: the difference is that the relative importance of the fluid perturbation is rather greater, and it is able to produce a much stronger barrier by locally reversing the viscosity perturbation. This is the first of the two physical mechanisms which are required for oscillations; the second is

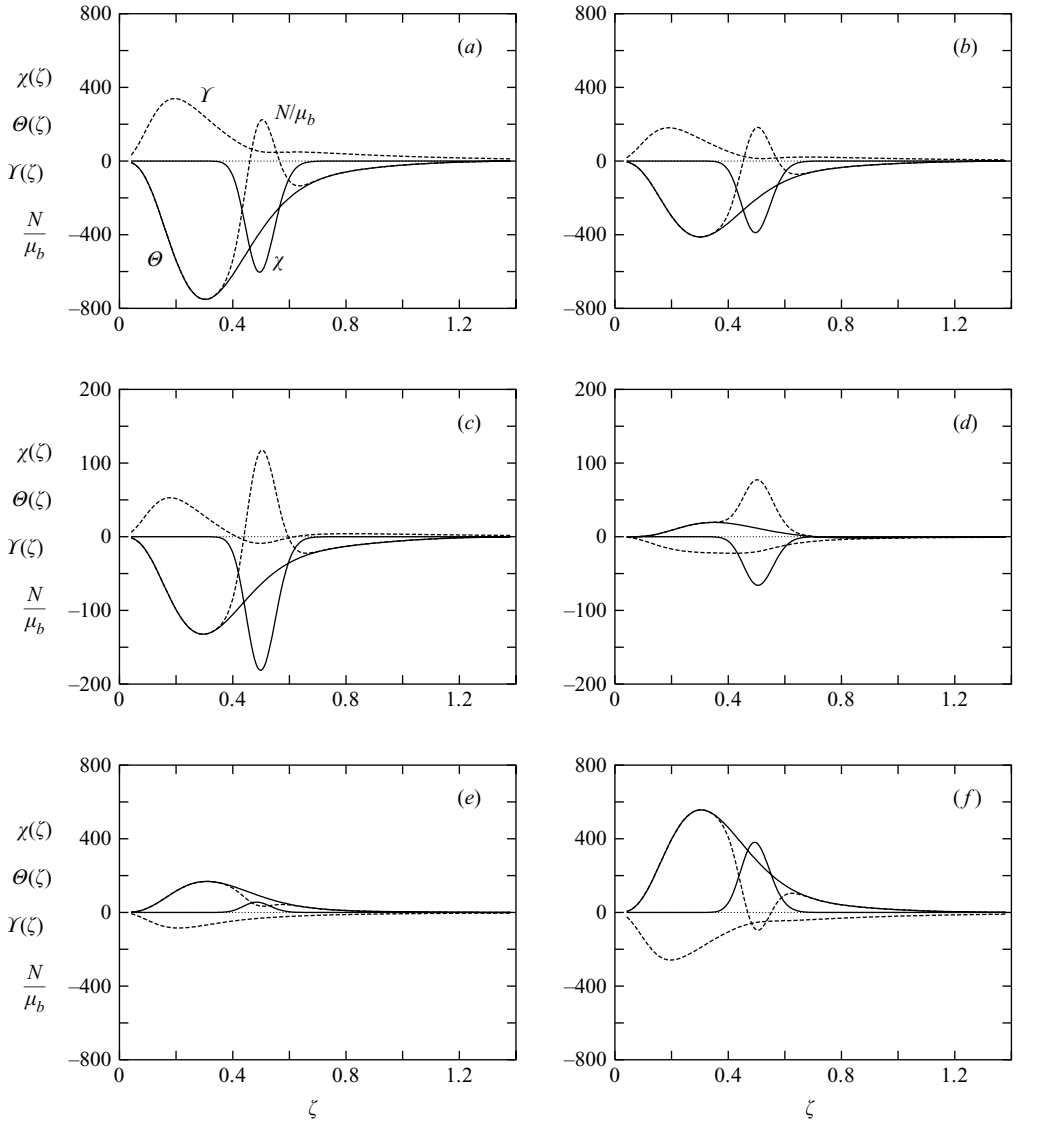

FIGURE 15. Evolving radial structure of most unstable perturbation for $P_c = 200$, $P_T = 10$, $\beta_c = 1$, $\beta_T = -10$, $\lambda = 0.75$ and $m = 5$ ($\nu = 0.343 + 0.172\,\mathrm{i}$). Solid lines represent solute perturbation $\chi(\zeta)$ and temperature perturbation $\Theta(\zeta)$ (exaggerated by a factor of 10 for clarity). Dashed lines represent viscosity perturbation $N(\zeta)/\mu_b(\zeta)$ and flux perturbation $\Upsilon(\zeta)$. All perturbations have been renormalized to remove the algebraic growth factor t^{ν_r}. 'Phase time' of snapshots: (*a*) $\tau = 0$; (*b*) $\tau = \pi/4$; (*c*) $\tau = 3\pi/8$; (*d*) $\tau = 7\pi/16$; (*e*) $\tau = \pi/2$; (*f*) $\tau = 11\pi/16$. Note smaller vertical scale in (*c*) and (*d*).

that because the solute perturbation $\chi(\zeta)$ is only weakly affected by diffusion, it responds more slowly to increases or decreases in the local velocity perturbation than the thermal perturbation $\Theta(\zeta)$ does. We recall that both of these mechanisms were absent in the 'thin-front' analysis of § 3, in which complex eigenvalues were impossible.

Figure 15 illustrates how these mechanisms operate. At $\tau = 0$ (figure 15*a*), the perturbation is sinuous. The negative thermal perturbation Θ leads to a mainly

negative viscosity perturbation N which in turn drives a positive flux perturbation Υ. However, this flux perturbation is restricted by the barrier of increased viscosity around the fluid front which is caused by the negative perturbation χ. Consequently, the flux is not sufficient to maintain the amplitude of the thermal and solute perturbations relative to the algebraic growth t^{ν_r}, and they both decay under diffusion ($\tau = \pi/4$, figure 15*b*). Being more affected by diffusion, the thermal perturbation decays faster, and so the relative importance of the viscosity barrier grows, accelerating the process further. By $\tau = 3\pi/8$ (figure 15*c*), the flux perturbation has reversed in the vicinity of the fluid front, and a little later ($\tau = 7\pi/16$, figure 15*d*), it has reversed everywhere. At this point, the thermal perturbation has also been reversed, but the solute perturbation has yet to follow suit. Consequently, both perturbations contribute a net increase in viscosity, which tends to amplify the now negative flux perturbation. A little time later ($\tau = \pi/2$, figure 15*e*), the positive thermal perturbation and the negative flux perturbation have each grown somewhat, reinforcing each other; the solute perturbation has now changed sign and it once again opposes the effect of the thermal perturbation, but is is still relatively weak compared to the thermal perturbation. As time goes on, both perturbations grow ($\tau = 11\pi/16$, figure 15*f*), but the solute perturbation grows faster because of the lower solute diffusion. Finally, by time $\tau = \pi$ the perturbation has completely inverted itself, and the process repeats.

6. Summary and conclusions

We have investigated the stability of the coupled thermal and fluid front system which results when fluid is injected from a line source into a thin horizontal saturated porous layer. When the viscosity of the fluid depends on both its composition and its temperature, viscous fingering may occur on either front, and a simplified model of the dynamics is sufficient to illustrate how the frontal instabilities couple, and how this coupling is controlled by the azimuthal wavelength m of the instability and by the relative thermal velocity λ.

The fingering instability on the thermal front is controlled by the diffusive redistribution of heat, and we have considered miscible fluids so that the instability on the fluid front is also controlled by diffusion. It is then possible to investigate the linear stability of the system by employing the eigenfunction decomposition method recently applied to miscible rectilinear displacements by Ben *et al.* (2002). This approach reveals that, in general, the linearized system possesses a discrete spectrum of eigenvalues corresponding to the growth rates of perturbations. The fastest-growing perturbations are dominated by a radial structure which corresponds to infinitesimally advancing or retarding the position of each front (cf. Barenblatt 1996, § 8.3). When the viscosity changes only across the fluid front, the growth rates of these most unstable perturbations agree with the results presented by Tan & Homsy (1987), and we have indicated how this analysis may be extended by a simple rescaling to cases in which the viscosity changes only across the thermal front.

When both fronts are unstable, the wavelength and growth rate of perturbations are controlled mainly by the properties of the fluid front, because of the much higher Péclet number associated with solute as opposed to thermal diffusion. However, when the thermal lag is not great and when the viscosity change across the thermal front is somewhat greater than that across the fluid front, the properties of the thermal

front may make a noticeable difference to the overall stability of the double-front system.

As for the 'thin-front' model considered by Cardoso & Woods (1995) and in § 3 of the current paper, the 'varicose' mode of instability in which the front perturbations are out of phase is substantially more stable than the 'sinuous' mode in which the perturbations are in phase. It is also strongly affected by diffusion, and decays strongly for large m.

When the fluid front is weakly unstable and the thermal front is stable, instabilities which are strongly localized about the fluid front can develop even when the viscosity profile is monotonically decreasing across the front, because of the different rates of advection of the fluid compositional properties and temperature. It is possible in principle for a weakly unstable fluid front to be stabilized by a sufficiently stable thermal viscosity gradient. However, the cases we have considered suggest that this effect is only significant for rather high values of the relative thermal velocity λ and when the thermal viscosity contrast is many times greater than the viscosity contrast across the fluid front. This has important practical applications, because it suggests that even when fluid is injected into a relatively warm medium (for example in the context of geothermal reservoir recharge), instabilities are likely to grow almost as fast as in the absence of the stabilizing temperature gradient.

The final case which we have considered occurs when the fluid front is weakly stable but the thermal front is unstable. In this case, the fluid front is generally unable to stabilize completely the instability centred on the thermal front; however, it provides a localized barrier to the developing velocity perturbation which can substantially affect the behaviour of the instability. A peculiar phenomenon which can result is an oscillatory instability (illustrated in figure 15), in which the maximum amplitude of the perturbations grows algebraically in time, but their sign varies. This behaviour depends crucially on the different rates of solute and thermal diffusion, which means that the perturbations to the fluid and thermal fronts take different times to respond to changes in the fluid velocity, and so a mild hysteresis effect is introduced.

The principal conclusion of this work is that for the stability of an injection process to be assessed, the viscosity changes associated with thermal and composition differences must be considered separately: in general, if either change promotes fingering, then an instability is likely to develop, although its rate of growth may be modified significantly by the coupling.

Since recent studies (e.g. French 2002; Jupp & Woods 2003) have considered reactions driven by thermal and compositional changes during injection processes, a natural extension of the current work would be to incorporate such reactions and the associated changes in fluid properties and the permeability of the porous matrix. Given the complex coupling revealed by the current analysis, and following recent studies of reaction-driven or -controlled instabilities (e.g. Chadam *et al.* 2001; de Wit 2001; Fernandez & Homsy 2003), we expect such coupled systems to exhibit a rich range of dynamics which will make them of considerable interest to the theoretician as well as to the chemical or petroleum engineer.

I am extremely grateful to Professor Andrew Woods for suggesting this study and for several stimulating and helpful discussions. I am also grateful to Professor Anthony Pearson and to two anonymous referees for their comments on the manuscript. This work was supported financially by the Newton Trust through the B. P. Institute.

Appendix A. Details of the thin-front stability analysis

The coefficients C_{ij} in equation (3.2) are given by

$$C_{11} = -\frac{1}{2} + \frac{1}{2}m(1-M_1)\frac{M_\infty(1+\lambda^m)+M_1(1-\lambda^m)}{M_1(1+M_\infty)(1+\lambda^m)+\left(M_\infty+M_1^2\right)(1-\lambda^m)}, \tag{A 1}$$

$$C_{12} = \frac{m\lambda^{(m+1)/2}(M_1-M_\infty)}{M_1(1+M_\infty)(1+\lambda^m)+\left(M_\infty+M_1^2\right)(1-\lambda^m)}, \tag{A 2}$$

$$C_{21} = \frac{m\lambda^{(m-1)/2}M_\infty(1-M_1)}{M_1(1+M_\infty)(1+\lambda^m)+\left(M_\infty+M_1^2\right)(1-\lambda^m)}, \tag{A 3}$$

$$C_{22} = -\frac{1}{2} + \frac{1}{2}m(M_\infty-M_1)\frac{(1+\lambda^m)+M_1(1-\lambda^m)}{M_1(1+M_\infty)(1+\lambda^m)+\left(M_\infty+M_1^2\right)(1-\lambda^m)} \tag{A 4}$$

(recall that $M_0 = 1$).

We may also show that the roots $\omega_\pm$ defined by equation (3.3) are real. The determinant in equation (3.3) can be written as

$$C_{11}^2 + C_{22}^2 - 2C_{11}C_{22} + 4C_{12}C_{21} = (M_1-M_\infty)^2(M_1-1)^2(\lambda^m-k_+)(\lambda^m-k_-), \tag{A 5}$$

where

$$k_\pm = \frac{M_1^2+M_\infty \pm 2M_1\sqrt{M_\infty}}{(M_1-M_\infty)(M_1-1)}. \tag{A 6}$$

The variable λ^m is constrained to be between 0 and 1, and the determinant is a concave parabola in λ^m; hence the range in which the determinant is negative lies between the roots $\lambda^m = k_\pm$, and we need to show that this interval does not overlap (0, 1). If one of the roots $k_\pm$ is greater than 0 while the other is less than 0, we must have $M_1^2 + M_\infty < 2M_1\sqrt{M_\infty}$, and by the triangle inequality this is impossible. Similarly, we can define

$$K_\pm = k_\pm - 1 = \frac{M_1(1+M_\infty \pm 2\sqrt{M_\infty})}{(M_1-M_\infty)(M_1-1)}, \tag{A 7}$$

and for one of these roots to lie on each side of 0, we would require $1 + M_\infty < 2\sqrt{M_\infty}$; again applying the triangle inequality, this is impossible. We conclude that whatever the ratio of mobilities, the radial structure introduced by diffusion is essential in this problem for the development of complex perturbation growth rates (see § 5.3.2).

Appendix B. Details of numerical methods

B.1. *Rescaling the eigenfunctions*

A natural definition of the prefactors G_j and H_j is to relate them to the inner products (4.20) and (4.22), and to define

$$G_j = P_T^{\lambda P_T/2+1}\frac{\Gamma(j+1)}{\Gamma\left(j+\frac{1}{2}\lambda P_T+1\right)}, \quad H_j = P_c^{P_c/2+1}\frac{\Gamma(j+1)}{\Gamma\left(j+\frac{1}{2}P_c+1\right)}. \tag{B 1}$$

These prefactors were used for small P_T and P_c. For high Péclet numbers, however, they become extremely small, and it is useful for computational purposes instead to

define

$$G_j = \frac{\mathrm{e}^{\lambda P_T/2}\Gamma(j+1)\Gamma\left(\frac{1}{2}\lambda P_T+1\right)}{\left(\frac{1}{2}\lambda\right)^{\lambda P_T/2}\Gamma\left(j+\frac{1}{2}\lambda P_T+1\right)} \quad \text{and} \quad H_j = \frac{\mathrm{e}^{P_c/2}\Gamma(j+1)\Gamma\left(\frac{1}{2}P_c+1\right)}{\left(\frac{1}{2}\right)^{P_c/2}\Gamma\left(j+\frac{1}{2}P_c+1\right)}. \tag{B 2}$$

B.2. *Shooting method for* $\varpi_p^T(\zeta)$

Equations (4.26) do not have closed-form solutions, and so must be integrated numerically for each set of parameter values. We develop asymptotic representations of $\varpi_p^T(\zeta)$ in each limit, with one free parameter in each, and use these to initialize the integrations at the points $\zeta_0 \ll 1$ and $\zeta_\infty \gg 1$; we then shoot inwards, adjusting the two free parameters so that ϖ_p^T and $\mathrm{d}\varpi_p^T/\mathrm{d}\zeta$ match at $\zeta = 1$. The numerical methods used were the globally convergent Newton's method and the Kaps–Rentop numerical integration routine suitable for stiff equations, as implemented by Press *et al.* (1992).

In the limit $\zeta \to \infty$, the terms $\partial T_b/\partial\zeta$, $\partial c_b/\partial\zeta$ and $\phi_p(\zeta)$ all become exponentially small, and it is simple to obtain the decaying solutions to equation (4.26),

$$\varpi_p^T(\zeta) \sim \Omega_\infty^T \zeta^{-m/2}, \tag{B 3}$$

for some constant Ω_∞^T which must be determined by shooting.

In the limit $\zeta \to 0$, the asymptotic order of the terms in equation (4.26) depends on the relative magnitudes of m, λP_T and P_c, and in general a series solution requires expansion in irregular powers of ζ. The leading-order term in such an expansion must be of the form

$$\varpi_p^T(\zeta) \sim \begin{cases} \Omega_0 \zeta^{m/2} & \text{if} \quad m < \lambda P_T \\ \Omega_0 \zeta^{m/2} - \frac{1}{4} m \beta_T L_0 \zeta^{m/2} \log\zeta & \text{if} \quad m = \lambda P_T \\ \dfrac{m^2 \beta_T L_0}{m^2 - \lambda^2 P_T^2} \zeta^{\lambda P_T/2} & \text{if} \quad m > \lambda P_T, \end{cases} \tag{B 4}$$

where $L_0 = L_p^{(\lambda P_T/2)}(0)$, and where Ω_0 is again to be obtained by shooting. Noting that we expect P_T in general to be a reasonably large quantity, we approximate ϖ_p^T near the origin as the sum of the terms proportional to $\zeta^{m/2}$ and $\zeta^{\lambda P_T/2}$, regardless of whether this is a formally correct expansion or not. By varying the points ζ_∞ and ζ_0 at which the boundary conditions are applied, we have confirmed that the shooting results do not depend sensitively on the handling of the boundary conditions.

An exactly analogous method was employed to calculate $\varpi_q^c(\zeta)$.

Appendix C. Inner products in the eigenvalue problem

We describe in detail only the construction of the evolution equations for the amplitudes $A_p^T(t)$, since the results for $A_q^c(t)$ follow immediately from these.

We take the inner product $\langle\cdot,\cdot\rangle_T$ of equation (4.8) with the radial eigenfunctions $\Phi_j(\zeta)$ for the temperature field. The time-derivative term gives

$$\left\langle t\frac{\partial\Theta}{\partial t}\ ,\ \Phi_j(\zeta)\right\rangle_T = \left\langle t\frac{\partial}{\partial t}\sum_{p=0}^{\infty} A_p^T(t)\Phi_p(\zeta)\ ,\ \Phi_j(\zeta)\right\rangle_T \tag{C 1}$$

$$= t\frac{\mathrm{d}A_j^T}{\mathrm{d}t}\langle\Phi_j,\Phi_j\rangle_T \tag{C 2}$$

$$= \frac{G_j^2}{P_T^{\lambda P_T/2+1}}\frac{\Gamma(j+\frac{1}{2}\lambda P_T+1)}{\Gamma(j+1)}\, t\frac{\mathrm{d}A_j^T}{\mathrm{d}t}. \tag{C 3}$$

The radial-derivative term gives

$$\langle \mathscr{L}_T \Theta \ , \ \Phi_j(\zeta) \rangle_T = \left\langle \mathscr{L}_T \sum_{p=0}^{\infty} A_p^T(t) \Phi_p(\zeta) \ , \ \Phi_j(\zeta) \right\rangle_T \tag{C 4}$$

$$= -j A_j^T \langle \Phi_j, \Phi_j \rangle_T \tag{C 5}$$

$$= -j \frac{G_j^2}{P_T^{\lambda P_T/2+1}} \frac{\Gamma(j + \frac{1}{2}\lambda P_T + 1)}{\Gamma(j+1)} A_j^T. \tag{C 6}$$

The azimuthal-derivative term gives

$$-\frac{1}{4}\frac{m^2}{P_T} \left\langle \frac{\Theta}{\zeta}, \Phi_j(\zeta) \right\rangle_T = -\frac{1}{4}\frac{m^2}{P_T} \left\langle \sum_{p=0}^{\infty} A_p^T(t) \frac{\Phi_p(\zeta)}{\zeta} \ , \ \Phi_j(\zeta) \right\rangle_T \tag{C 7}$$

$$= -\frac{1}{4}\frac{m^2}{P_T} \sum_{p=0}^{\infty} A_p^T(t) \int_0^{\infty} G_j G_p \mathrm{e}^{-P_T\zeta} \zeta^{\lambda P_T/2-1} L_p^{(\lambda P_T/2)}(P_T\zeta) L_j^{(\lambda P_T/2)}(P_T\zeta) \, \mathrm{d}\zeta, \tag{C 8}$$

and by expanding the Laguerre polynomials we obtain

$$-\frac{1}{4}\frac{m^2}{P_T} \left\langle \frac{\Theta}{\zeta}, \phi_j(\zeta) \right\rangle_T = -\frac{1}{4}\frac{m^2}{P_T} \sum_{p=0}^{\infty} P_T^{-\lambda P_T/2} D_{j,p}^T G_j G_p A_p^T(t), \tag{C 9}$$

where

$$D_{j,p}^T = \Gamma\left(p + \frac{1}{2}\lambda P_T + 1\right) \Gamma\left(j + \frac{1}{2}\lambda P_T + 1\right) \times \sum_{r=0}^{p} \frac{\sum_{s=0}^{j} \frac{(-1)^{r+s} \Gamma\left(r + \frac{1}{2}\lambda P_T + s\right)}{\Gamma(j-s+1)\Gamma\left(s + \frac{1}{2}\lambda P_T + 1\right)\Gamma(s+1)}}{\Gamma(p-r+1)\Gamma\left(r + \frac{1}{2}\lambda P_T + 1\right)\Gamma(r+1)}$$

$$= \frac{2}{\lambda P_T} \frac{\Gamma\left(J + \frac{1}{2}\lambda P_T + 1\right)}{\Gamma(J+1)}, \tag{C 10}$$

where $J = \min(j, p)$. Finally, we consider the term which corresponds to the advective transport of heat,

$$-\frac{1}{2}\frac{\lambda}{K_T} \left\langle \Upsilon(\zeta, t) \mathrm{e}^{-P_T\zeta} \zeta^{\lambda P_T/2-1}, \Phi_j(\zeta) \right\rangle_T$$

$$= -\frac{1}{2}\frac{\lambda}{K_T} \left\langle \left(\sum_{p=0}^{\infty} A_p^T(t) \varpi_p^T(\zeta) + \sum_{q=0}^{\infty} A_q^c(t) \varpi_q^c(\zeta) \right) \mathrm{e}^{-P_T\zeta} \zeta^{\lambda P_T/2-1}, \Phi_j(\zeta) \right\rangle_T. \tag{C 11}$$

The inner product can be written as

$$\left\langle \Upsilon(\zeta, t) \mathrm{e}^{-P_T\zeta} \zeta^{\lambda P_T/2-1}, \Phi_j(\zeta) \right\rangle_T = \sum_{p=0}^{\infty} G_j I_{j,p}^T A_p^T(t) + \sum_{q=0}^{\infty} G_j I_{j,p}^c A_q^c(t), \tag{C 12}$$

where the coefficients $I^T_{j,p}$ and $I^c_{j,p}$ are defined as

$$I^T_{j,p} = \int_0^\infty \mathrm{e}^{-P_T\zeta}\zeta^{\lambda P_T/2-1}L_j^{(\lambda P_T/2)}(P_T\zeta)\varpi_p^T(\zeta)\,\mathrm{d}\zeta, \tag{C 13}$$

$$I^c_{j,p} = \int_0^\infty \mathrm{e}^{-P_T\zeta}\zeta^{\lambda P_T/2-1}L_j^{(\lambda P_T/2)}(P_T\zeta)\varpi_p^c(\zeta)\,\mathrm{d}\zeta. \tag{C 14}$$

The quantities $I^T_{j,p}$ and $I^c_{j,p}$ must be evaluated numerically along with the functions $\varpi_p^{T,c}(\zeta)$.

In a similar fashion, we take the inner product $\langle\cdot,\cdot\rangle_c$ of equation (4.9) with the eigenfunctions $\Psi_j(\zeta)$, obtaining the terms

$$\left\langle t\frac{\partial\chi}{\partial t}\ ,\ \Psi_j(\zeta)\right\rangle_c = \frac{H_j^2}{P_c^{P_c/2+1}}\frac{\Gamma\left(j+\frac{1}{2}P_c+1\right)}{\Gamma(j+1)}\,t\frac{\mathrm{d}A^c_j}{\mathrm{d}t}; \tag{C 15}$$

$$\langle\mathscr{L}_c\chi\ ,\ \Psi_j(\zeta)\rangle_c = -j\frac{H_j^2}{P_c^{P_c/2+1}}\frac{\Gamma\left(j+\frac{1}{2}P_c+1\right)}{\Gamma(j+1)}\,A^c_j; \tag{C 16}$$

$$-\frac{1}{4}\frac{m^2}{P_c}\left\langle\frac{\chi}{\zeta},\Psi_j(\zeta)\right\rangle_c = -\frac{1}{4}\frac{m^2}{P_c}\sum_{p=0}^\infty P_c^{-P_c/2}H_jH_pD^c_{j,p}A^c_p(t) \tag{C 17}$$

for

$$D^c_{j,p} = \frac{2}{P_c}\frac{\Gamma\left(J+\frac{1}{2}P_c+1\right)}{\Gamma(J+1)}, \tag{C 18}$$

where $J=\min(j,p)$ as before; and finally,

$$-\frac{1}{2K_c}\left\langle\Upsilon(\zeta,t)\mathrm{e}^{-P_c\zeta}\zeta^{P_c/2-1},\Psi_j(\zeta)\right\rangle_c = -\frac{1}{2K_c}\left(\sum_{p=0}^\infty H_jJ^T_{j,p}A^T_p(t)+\sum_{q=0}^\infty H_jJ^c_{j,p}A^c_q(t)\right), \tag{C 19}$$

where

$$J^T_{j,p} = \int_0^\infty \mathrm{e}^{-P_c\zeta}\zeta^{P_c/2-1}L_j^{(P_c/2)}(P_c\zeta)\varpi_p^T(\zeta)\,\mathrm{d}\zeta, \tag{C 20}$$

$$J^c_{j,p} = \int_0^\infty \mathrm{e}^{-P_c\zeta}\zeta^{P_c/2-1}L_j^{(P_c/2)}(P_c\zeta)\varpi_p^c(\zeta)\,\mathrm{d}\zeta. \tag{C 21}$$

Combining these expressions, we obtain the coupled amplitude evolution equations (4.27), where the coefficients $Q^{kl}_{j,p}$, where $k,l=T$ or c, are given by

$$Q^{TT}_{j,p} = -j\,\delta_{j,p} - \frac{\Gamma(j+1)}{\Gamma\left(j+\frac{1}{2}\lambda P_T+1\right)}\left[\frac{m^2}{4}\frac{G_p}{G_j}D^T_{j,p}+\frac{P_T^{\lambda P_T/2+1}}{G_j}\frac{\lambda}{2K_T}I^T_{j,p}\right], \tag{C 22}$$

$$Q^{Tc}_{j,p} = -\frac{\Gamma(j+1)}{\Gamma\left(j+\frac{1}{2}\lambda P_T+1\right)}\frac{P_T^{\lambda P_T/2+1}}{G_j}\frac{\lambda}{2K_T}I^c_{j,p}, \tag{C 23}$$

$$Q^{cT}_{j,p} = -\frac{\Gamma(j+1)}{\Gamma\left(j+\frac{1}{2}P_c+1\right)}\frac{P_c^{P_c/2+1}}{H_j}\frac{1}{2K_c}J^T_{j,p}, \tag{C 24}$$

$$Q^{cc}_{j,p} = -j\,\delta_{j,p} - \frac{\Gamma(j+1)}{\Gamma\left(j+\frac{1}{2}P_c+1\right)}\left[\frac{m^2}{4}\frac{H_p}{H_j}D^c_{j,p}+\frac{P_c^{P_c/2+1}}{H_j}\frac{1}{2K_c}J^c_{j,p}\right]. \tag{C 25}$$

REFERENCES

Arfken, G. B. & Weber, H.-J. 1995 *Mathematical Methods for Physicists* 2nd edn. Academic.

Azaiez, J. & Singh, B. 2002 Stability of miscible displacements of shear thinning fluids in a Hele-Shaw cell. *Phys. Fluids* **14**, 1557–1571.

Barenblatt, G. I. 1996 *Scaling, Self-Similarity and Intermediate Asymptotics*. Cambridge University Press.

Bear, J. 1972 *Dynamics of Fluids in Porous Media*. Dover.

Ben, Y., Demekhin, E. A. & Chang, H.-C. 2002 A spectral theory for small-amplitude miscible fingering. *Phys. Fluids* **14**, 999–1010.

Cardoso, S. S. S. & Woods, A. W. 1995 The formation of drops through viscous instability. *J. Fluid Mech.* **289**, 351–378.

Chadam, J., Ortoleva, P., Qin, Y. & Stamicar, R. 2001 The effect of hydrodynamic dispersion on reactive flows in porous media. *Eur. J. Appl. Maths* **12**, 557–569.

Fernandez, J. & Homsy, G. M. 2003 Viscous fingering with chemical reaction: effect of *in situ* production of surfactants. *J. Fluid Mech.* **480**, 267–281.

French, A. 2002 Precipitation and dissolution reactions in porous media. M.Phil. thesis, University of Cambridge.

Homsy, G. M. 1987 Viscous fingering in porous media. *Annu. Rev. Fluid Mech.* **19**, 271–311.

Jupp, T. E. & Woods, A. W. 2003 Thermally-driven reaction fronts in porous media. *J. Fluid Mech.* **484**, 329–346.

Latil, M. 1980 *Enhanced Oil Recovery*. Éditions Technip.

Manickam, O. & Homsy, G. M. 1993 Stability of miscible displacements in porous media with nonmonotonic viscosity profiles. *Phys. Fluids* A **5**, 1356–1367.

Manickam, O. & Homsy, G. M. 1995 Fingering instabilities in vertical miscible displacement flows in porous media. *J. Fluid Mech.* **288**, 75–102.

Miranda, J. M. & Widom, M. 1998 Radial fingering in a Hele-Shaw cell: a weakly nonlinear analysis. *Physica* D **120**, 315–328.

Paterson, L. 1981 Radial fingering in a Hele-Shaw cell. *J. Fluid Mech.* **113**, 513–529.

Phillips, O. M. 1991 *Flow and Reactions in Permeable Rocks*. Cambridge University Press.

Press, W. H., Teukolsky, S. A., Vetterling, W. T. & Flannery, B. P. 1992 *Numerical Recipes in Fortran 77* 2nd edn. Cambridge University Press.

Riaz, A. & Meiburg, E. 2003 Radial source flows in porous media: linear stability analysis of axial and helical perturbations in miscible displacements. *Phys. Fluids* **15**, 938–946.

Rogerson, A. & Meiburg, E. 1993 Shear stabilisation of miscible displacement processes in porous media. *Phys. Fluids* A **5**, 1344–1355.

Saffman, P. G. & Taylor, G. I. 1958 The penetration of a fluid into a porous medium or Hele–Shaw cell containing a more viscous liquid. *Proc. R. Soc. Lond.* A **245**, 312–329.

Somerton, W. H. 1992 *Thermal Properties and Temperature-related Behaviour of Rock-Fluid Systems*. Elsevier.

Stefánsson, V. 1997 Geothermal reinjection experience. *Geothermics* **26**, 99–139.

Tan, C. T. & Homsy, G. M. 1986 Stability of miscible displacements in porous media: rectilinear flow. *Phys. Fluids* **29**, 3549–3556.

Tan, C. T. & Homsy, G. M. 1987 Stability of miscible displacements in porous media: radial source flow. *Phys. Fluids* **30**, 1239–1245.

Turner, J. S. 1979 *Buoyancy Effects in Fluids*. Cambridge University Press.

de Wit, A. 2001 Fingering of chemical fronts in porous media. *Phys. Rev. Lett.* **87**, 87.054502.

Woods, A. W. 1999 Liquid and vapour flow in superheated rock. *Annu. Rev. Fluid Mech.* **31**, 171–199.

Woods, A. W. & Fitzgerald, S. D. 1997 The vaporization of a liquid front moving through a hot porous rock. *J. Fluid Mech.* **343**, 303–316.